Observations on the influence of process and corrosion related defects on the fatigue strength of 316L stainless steel manufactured by Laser Powder Bed Fusion (L-PBF).

Pierre MEROT[a,b], Franck MOREL[a], Linamaria GALLEGOS MAYORGA[a], Etienne PESSARD[a], Paul BUTTIN[b], Thierry BAFFIE[c]

[a] *LAMPA (EA1427), Arts et Métiers, Angers, FRANCE*
[b] *CEA, CTREG, DGDO, Bouguenais, FRANCE*
[c] *CEA-LITEN, Univ.Grenoble Alpes, Grenoble, FRANCE*

Abstract

Corrosive environments are known to be detrimental to the mechanical strength of metallic alloys. In the case of 316L stainless steel, the main corrosion mechanism observed is pitting, which leads to localized rough defects. As for other materials submitted to cyclic loadings and prone to pit, corrosion defects tend to be at the core of crack initiation leading to failure. The work here-by presented will thus focus on the relationship between the fatigue performance and the presence of process or corrosion related defects for a 316L stainless steel manufactured by Laser Powder Bed Fusion (L-PBF). To do so, cylindrical samples were produced vertically, then machined to fatigue specimens in as-built state (no heat treatment). Specimens were polished in order to only characterize the bulk material and not its raw surface. The fatigue responses of three batches corresponding to three configurations of surface integrity (polished, pre-corroded and with an Electric Discharge Machined (EDM) defect) were investigated. For the polished batch, fracture surface observations showed that initiation started from a lack of fusion (LoF) surface pore in all specimens. The pre-corroded batch was prepared under potentiodynamic anodic polarization conditions in a neutral NaCl solution. On those samples, some cracks initiated on corrosion pits, depending on the severity of the corrosion applied to each sample and its initial population of defects. For the EDM batch, a hemispherical defect, at the source of all failures, was machined in the middle of the gauge length. A good correlation between Murakami's $\sqrt{area}$ parameter and the fatigue strength was observed on a Kitagawa-Takahashi diagram for all tested specimens. This correlation showed an independence of the defect type (LoF, pit, machined defect) on the specimens fatigue strength. Defect morphology doesn't seem to be an important driving force for crack initiation as ellipsoidal corrosion pits, hemispherical EDM defects and flat lacks of fusion, although very different in terms of shape, are just as harmful at equivalent sizes.

Keywords: 316L Stainless Steel, Laser Powder Bed Fusion (L-PBF), Fatigue, High Cycle Fatigue (HCF), Defects, Crack initiation, Corrosion, Pitting corrosion

1. Introduction

Additive Manufacturing (AM) has become a subject of interest for researchers since this process is now widely used in the industry [10, 16, 41]. Laser Powder Bed Fusion (L-PBF) is one of the most common AM technologies applied on metals [16, 17, 45]. It enables to build highly dense and complex parts, which until then, could not be produced with conventional processes [54]. L-PBF is then particularly relevant for small series and/or high added value parts.

Numerous studies about L-PBF 316L have been conducted in order to characterize its microstructure, and to compare its mechanical properties with conventionally-built 316L pieces. This alloy is commonly used in biomedical, marine, automotive and construction industries [34, 35, 49]. Its high corrosion resistance and relatively good mechanical properties make this material suitable in many applications [35, 49, 53]. One of its main observed features is the typical microstructure resulting from the L-PBF process. Due to the extremely fast cooling of the laser melted zone (5×10^5 - 4×10^7 K/s) and the orientation of the thermal gradient in the part and its intensity (2×10^6 - 2.6×10^7 K/m), the manufactured material is composed by

a mix of fine equiaxed grains and long columnar grains [6, 7, 22]. The columnar grains grow through the powder layers with a length in the range of tens to hundreds of microns parallel to the building direction. Equiaxed grains size range and columnar grains width are both in the order of ten microns [28, 41]. At a lower scale, solidification cells in the range of hundreds of nanometers to a few microns could be observed inside the grains [34, 39]. A high density of dislocations was revealed on cells walls, in contrast with cells interiors [50]. It's worth noting that some precipitates and impurities can be found on the cell boundaries creating local chemical variations in the material [43, 48, 50].

Another well known feature typical of the L-PBF process is the presence of defects in the manufactured parts. Indeed, altough AM processes parameters are optimized (an almost fully dense material is produced), such defects are currently unavoidable [56]. The most common amongst them are gas pores, lack of fusion pores (LoF), cracks, delaminations and balling effect related defects [29, 17, 39]. Depending on the application, such defects could be an important issue and should be taken into account for parts design.

In-service parts can be submitted to various types of external stresses. In the maritime field, corrosion and mechanical solicitations are the most detrimental to structural integrity. L-PBF 316L corrosion behaviour has been extensively studied by researchers [21, 34]. As for every stainless steel, the high corrosion resistance of the L-PBF 316L is due to a protector chromium Cr based passive film formed at the surface of the piece. Uniform corrosion is prevented, but in chloride Cl containing environment, localized corrosion, such as pitting corrosion, may occur because of the adsorption of Cl^- anion by the passive film, leading to its breakdown [5, 8, 32]. Once a pit is nucleated, if the electrochemical conditions allow it, a pit can grow very fast which makes this type of defect highly noxious for the component integrity. The corrosion behaviour comparison between L-PBF and wrougth 316L is still unclear in the literature because of the lack of a standard for the L-PBF process. However, some authors observed better corrosion resistance for the L-PBF material than for the wrougth one. This higher corrosion resistance is mainly reported to be the result of the high solidification rates (0.2 - 3.8 m/s) [6] of the material during the L-PBF processing, preventing the formation of non-metallic inclusions such as MnS which are known to be strong pit initiators [4, 20, 26]. Some studies highlighted as well the possible role of the fine microstructure resulting from the L-PBF process. Indeed, it could be responsible of an increase in the strength of the passive film, but also, a reduction in pit penetration [2, 24, 25].

On the other hand, L-PBF quasi-static behaviour is reported to be at least as good as its wrougth counterpart. It is now well accepted that it is mainly due the fine microstructure generated by the AM process (hall-petch effect) [42, 51, 54]. The oriented columnar grains are also the source of the anisotropic mechanical behaviour of the material [54]. However, these good static mechanical properties are partially occulted in the High Cycle Fatigue regime (HCF) because of the presence of L-PBF defects known to be detrimental to fatigue resistance. Indeed, crack initiations were observed to occur on lack of fusion sites, or at cluster of defects zones, near the sample surface [9, 56].

When L-PBF 316L is used in a corrosive environment, corrosion pits may be added to the fabrication process related population of defects. Several studies showed that pits could be critical in the HCF regime, as cracks initiation on these defects were observed [19, 30, 55]. A competition between different types of defects on the fatigue strength of the material is thus a possibility. The corrosion fatigue coupling could also be particularly harmful for some materials [13, 30, 52]. Different coupling mechanisms were pointed out in the literature, such as local persistent slip bands inducing pit initiation [14, 23], loading driving pit growth morphology [40, 52], corrosion at crack tip [31] or hydrogen embrittlement [11]. These coupling mechanisms could potentially decrease the lifetime more drastically than it could be predicted by considering corrosion and fatigue phenomena independently.

However, before studying corrosion-fatigue coupling, independent contributions of these two external damage sources must be quantified. In this paper, the effect of defects of different types on the fatigue strength of L-PBF 316L was studied. In order to qualify these effects, fatigue tests were carried out. Three different surface integrity conditions were investigated : polished (machined + polished), pre-corroded (machined + polished + pre-corroded) and with an Electric Discharge Machined (EDM) defect (machined + polished + hemispherical EDM defect). These three conditions were tested in order to generate various types of defects

on the fatigue specimens : L-PBF pores only in the polished condition, L-PBF pores + corrosion pits in the pre-corroded condition and L-PBF pores + one hemispherical defect for the EDM defect condition. By means of comparing these three specimen configurations, the following questions were considered :

- How much does corrosion affect the fatigue strength of the material ?
- Are there interactions between corrosion pits and L-PBF pores ?
- Is there a competition between defects of different nature for crack initiation ?
- Could we describe the criticality of a defect independently of its nature, with morphological parameters such as the defect size ?

2. Material and experimental conditions

2.1. Material chemical composition

The material used in the present work is a 316L grade stainless steel. It was received as powder (10-45 μm), in several batches provided by TLS Technik, then, manufactured using the L-PBF process. The L-PBF bulk material chemical composition was verified using Instrumental Gas Analysis (IGA) and Inductively Coupled Plasma Mass Spectrometry (ICP-MS) methods. These measurements were conducted by Elektrowerk Weisweiler on six different samples. The mean value of the 6 measurements on the bulk samples (i.e. the manufactured L-PBF material) is shown in table 1. The EN 10028-7 standard [1] for 316L stainless steel was respected. The density of the powder was measured with a helium gas pycnometer. After one hundred measures, the mean value was found equal to $\rho_{powder} = 7.893\ g/cm^3$, with a standard deviation of $2.1 \times 10^{-3}\ g/cm^3$.

	C (wt%)	O (wt%)	N (wt%)	Cr (wt%)	Mn (wt%)	Mo (wt%)	Ni (wt%)	P (wt%)	S (wt%)	Si (wt%)
EN 10 028-7 [1]	$\leqslant 0.03$	< 0.1	$\leqslant 0.1$	16.5-18.5	$\leqslant 2$	2-2.5	10-13	$\leqslant 0.045$	$\leqslant 0.015$	$\leqslant 1$
TLS bulk	0.013	0.054	0.058	16.99	0.88	2.26	11.19	0.005	0.004	0.63

Table 1: Chemical composition of the L-PBF 316L samples compared to the EN 10028-7 standard [1].

2.2. L-PBF fabrication and material tensile properties

All the mechanically tested specimens were vertically built under Nitrogen (N) atmosphere using a Farsoon FS271M L-PBF machine (figure 1 (a)). The oxygen weight ratio in the fabrication chamber was smaller than 0.25 %. A laser power of 225 W, with a laser scan speed of 1000 mm/s and a layer thickness of 30 μm were used. A stripes filling strategy was adopted, with a stripe width of 10 mm, an overlap between stripes of 70 μm and a hatch of 90 μm (figure 1 (d)). A rotation of 67 ° of the scan pattern was performed between powder layers (figure 1 (c)). For the contours, a laser power of 140 W and a laser scan speed of 500, 800 and 500 mm/s for upskin, downskin and standard contours respectively were used. In order to build all the samples, 5 different plates were manufactured (figure 1 (b)).

The typical microstructure of the as-built material after etching is showed in figure 2. The superposition of melted pool and some elongated grains parallel to the building direction (BD) (figure 2 (a)) can be observed. Some other process parameters such as the hatch and the scan pattern rotation could be seen through the laser path traces (figure 2 (b)). The density of the as-built material was measured by SEM image analyses. The results indicated a density higher than 99.9% for each considered scans. It indicated qualitatively a good macroscopic material health. Density measurements using Archimedes' principle were performed and values were in good agreement with image analyses results.

Seven tensile tests were also carried out on vertically built samples. To highlight the influence of the particular microstructure resulting from the L-PBF manufacturing, three of the tensile samples were heat treated (1050 °C for 30 min under vacuum, N_2 - H_2 quenching under 3-4 bar). The results of these tensile

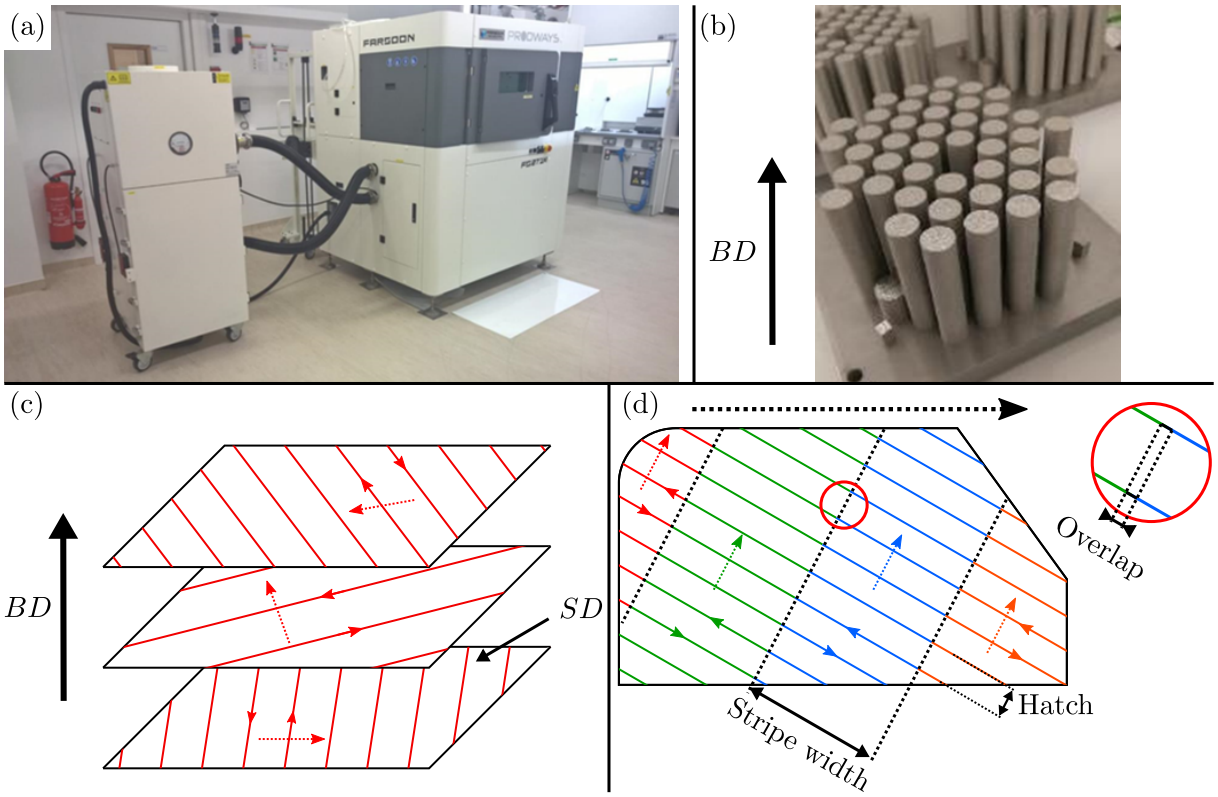

Figure 1: L-PBF additive manufacturing process, with (a) the L-PBF machine used, (b) an example of a fatigue samples plate, (c) a scheme of the scanning pattern rotation (BD : Building Direction, SD : Scan Direction) and (d) an illustration of different filling strategy parameters.

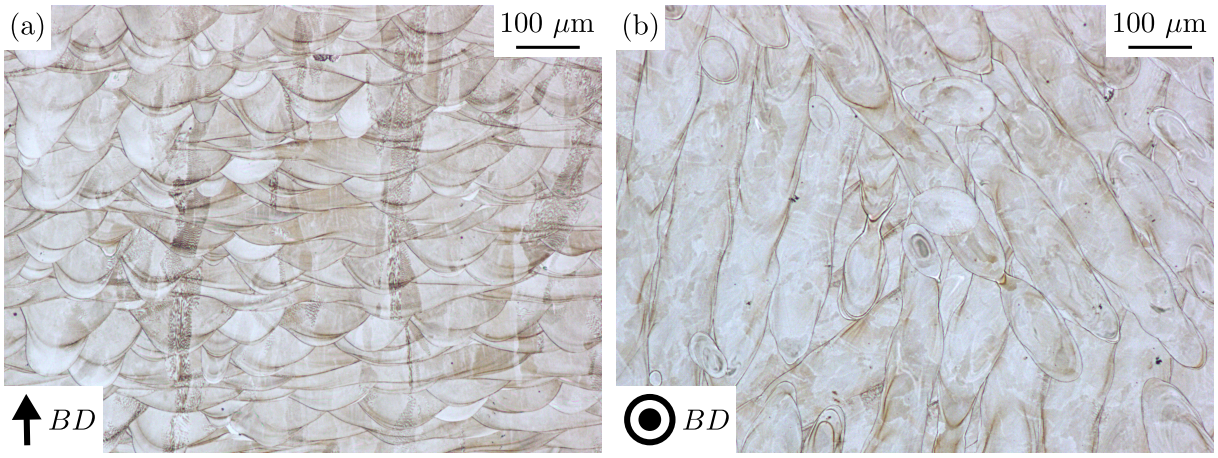

Figure 2: 316L FLLP typical microstructure observed with optical microscope after etching.

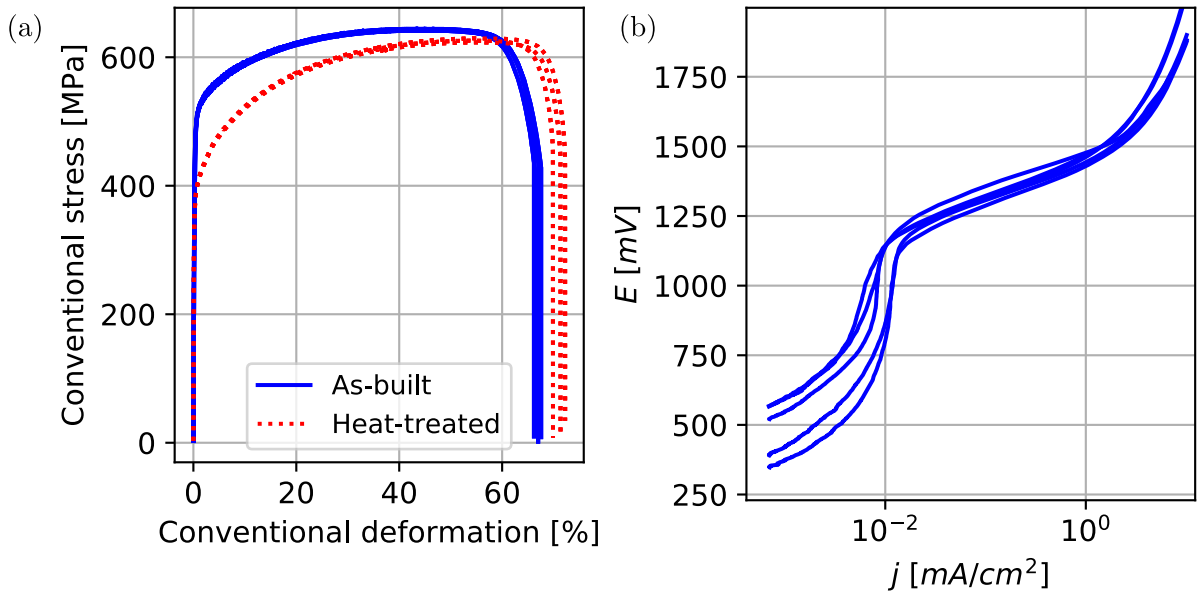

Figure 3: (a) Tensile behaviour of L-PBF 316L as-built (AB) and heat treated (H) and (b) anodic polarization behaviour of L-PBF 316L as-built (AB).

tests are plotted figure 3 (a) and summarized in table 2. The ultimate tensile stress is almost identical for as-built, heat-treated and wrought conditions [18]. On the other hand, the yield stress is higher in the as-build condition in comparison to the heat-treated material, with a ratio $YS_{as-built}/YS_{heat-treated} = 1.28$. This is mainly due to the very fine microstructure resulting of the high cooling rate during L-PBF process [17]. The heat-treated material yield stress is close to the wrought one, a full recrystallization may have occured, resulting in bigger equiaxed grains, and the disappearance of cells features [2, 33, 42].

2.3. Fatigue batches preparation

The vertical fatigue specimens were kept in their as-build condition (i.e without heat-treatment). After the L-PBF process, and to solely characterise the inner volume of the material, the samples were machined, then manually polished to avoid machining artefacts. The fatigue sample geometry is given in figure 4.

To observe the sensitivity of the material to different types of defects, three surface conditions were studied : (i) without any other operation (machined + polished only), noted as "polished air" (ii) corroded with anodic polarization, noted as "pre-corroded air" (iii) EDM specimens on which one hemispherical defect was

Batch	UTS (MPa)	YS (MPa)	El.% (%)	E (GPa)
As-built	642	484	67	227
Heat-treated	626	377	71	236
Wrought [18]	644	346	60	/

Table 2: Tensile tests results for as-built and heat-treated L-PBF 316L compared to wrought 316L [18].

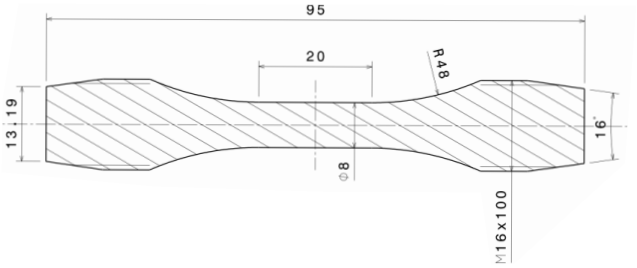

Figure 4: Fatigue sample geometry (dimensions in mm).

introduced on the middle of the gauge length, noted as "EDM defect air". Six EDM defect specimens were tested in this study. The diameters of the introduced defects in the specimens were of 400, 600, and 800 μm (with two specimens per diameter), corresponding respectively to 251, 376 and 501 μm in terms of the square root of the projected area of the defect on a plane perpendicular to the loading direction $\sqrt{area}$, as defined by Murakami and Endo [38]. Figure 5 represents the global process for batches preparation, from the building plate to final specimen geometry.

Pre-corrosion was performed at room temperature ($\approx$ 20 °C) in an aqueous saline neutral solution, with a NaCl concentration $c(NaCl) = 50 \pm 5$ g/L and a pH maintained between 6.5 and 7.2 by adding sodium hydroxyde $NaOH$ in the solution. A Origalys 4 electrodes cell was used (figure 6), with a satured calomel electrode (SCE) as reference, a platinum grid counter electrode (CE), an auxiliary electrode (Aux) and the fatigue specimen taking the working electrode place (WE). To avoid corrosion product dripping along the specimen surface (due to gravity), a magnetic agitator was used to force particles extraction from the corrosion pits. To prevent corrosion on the immersed threaded end of the sample, a thin coat of paraffin wax was applied to it. Once immersed in the solution, at least 1 hour of open circuit potential was performed to ensure free potential stabilization. Then, a potentiodynamic polarization was applied, starting from the previously measured free potential (E_{free}) to a maximum potential (E_{max}) corresponding to a fixed maximum current density ($j_{max} \in [5, 10]\ mA/cm^2$), with a scan rate of 1 mV/s. The potential was then maintained during $t \in [0, 20]\ min$. Figure 3 (b) shows typical anodic polarization responses of our material in these conditions. It can be noticed that at $pH = 7$, when the potential exceeds 810 mV, the system is no more in the stability domain of the water. The current intensity experimentally measured is then the sum of the metal corrosion and the water dissociation reactions contributions. Different distributions of pits (in terms of number and size) were generated using this process.

Figure 7 gives an overview of two planar samples (a) Corr1 and (b) Corr2 after corrosion. These two samples were built on the same plates as fatigue specimens (with exactly the same powder and building parameters and similar raw geometry). The use of planar samples was chosen to simplify the performance of a SEM scan. After defects segmentations on the raw images from both SEM scans, the total cumulative defects distribution sizes in terms of square root of the defect area ($P_{Si}(x < \sqrt{area})$) was processed for each sample on its respective scan area S_i. A correction was then applied to represent the cumulative defect distribution on a constant surface area $P_{S0}(x < \sqrt{area})$, with $S_0 = 1\ cm^2$, using equation 1.

$$P_{S0}(x < \sqrt{area}) = P_{Si}(x < \sqrt{area})^{S_0/S_i} \tag{1}$$

The normalised cumulative distributions of defects sizes for the 50 biggest defects observed are significantly different (figure 7 (c)). All surface defects bigger than $\sqrt{area} = 1$ μm were considered in the segmentation. Because corrosion pits were the biggest defects, the focus was on defects bigger than $\sqrt{area} = 60$ μm, which was the median size of the critical LoF defect in our fatigue specimens, as it is discussed further in this paper. For Corr1 sample, 35 defects bigger than $\sqrt{area} = 60$ μm (probably only corrosion pits) were found, whereas

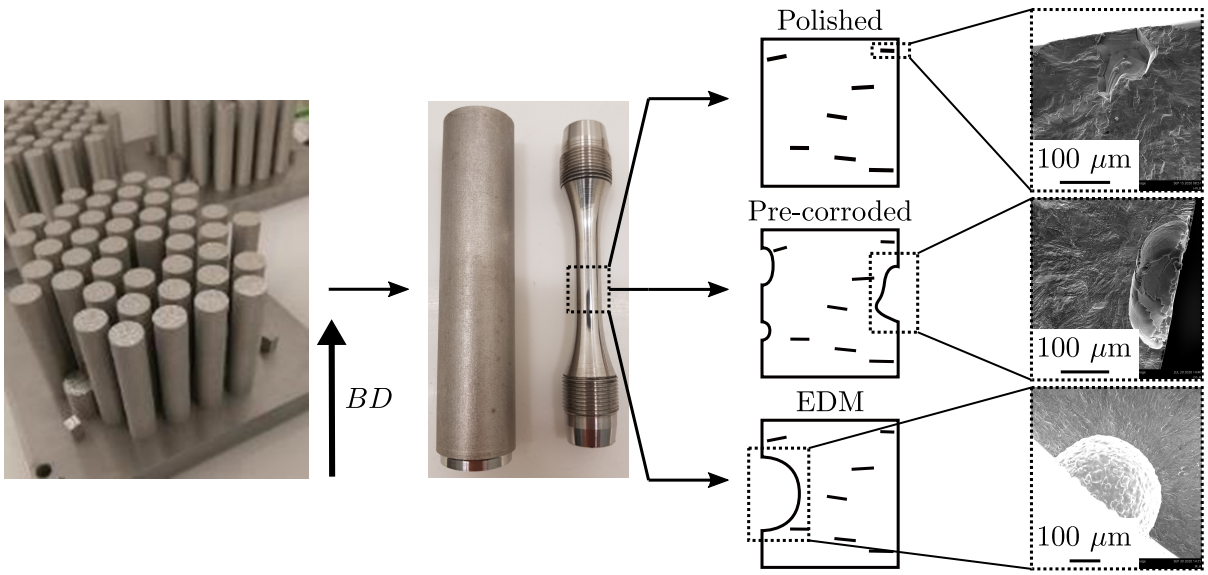

Figure 5: Different steps of the fabrication of the different tested batches. The SEM fractographies show 1 LoF, 1 corrosion pit and 1 hemispherical EDM defects.

only 5 were observed on sample Corr2. However, the biggest corrosion pit is on sample Corr2 with a size around $\sqrt{area} = 450$ μm, which is more than twice the size of the largest pit (around $\sqrt{area} = 200$ μm) on sample Corr1. The two populations observed were clearly different, particularly in terms of large defects, which was the main goal using this pre-corrosion set-up.

In the current paper, the pit distribution was considered as a stochastic variable, which could not be determined before observation of the corroded specimen. Due to the cylindrical geometry of the fatigue specimen, the SEM scanning process of the sample, as shown figures 7 (a) and (b), is more difficult to perform than for planar specimens. Figure 8 shows a typical example of a fatigue specimen surface topography after pre-corrosion.

The main objective of this pre-corrosion process is to introduced various pit populations on the fatigue specimens. This is naturally achieved because of the stochastic nature of pitting phenomenon, even at fixed electrochemical parameters. Even if the global defect population is not established before the fatigue test, the critical defect can still be analysed after sample failure (as discussed in subsection 3.2).

2.4. Fatigue testing conditions

Fatigue tests were carried out using a MTS Landmark 100 kN servohydraulic fatigue test machine. The tests were conducted at room temperature (≈ 20 °C) in air. A fully alternative uniaxial load ($R = -1$), at a frequency of 15 Hz for stresses lower than 350 MPa and 1 Hz (to avoid specimen self-heating) otherwise, was applied. Load control mode was used. A step by step method was used, with $\Delta N = 10^6$ cycles per step, and increasing the stress amplitude by 25 MPa between steps. Each test was carried out up to fracture. For each sample, fatigue failure surfaces were analysed using a Phenom XL SEM microscope. The defect responsible for the crack initiation was then characterized. Examples of these characterizations are given figure 10. The summary of the tested batches is reported table 3.

Batch	Surface integrity	Number of specimens
Polished	Polished	23
Pre-corroded	Polished + pre-corroded	34
EDM defect	Polished + EDM defect	6

Table 3: Summary of the tested batches in fatigue.

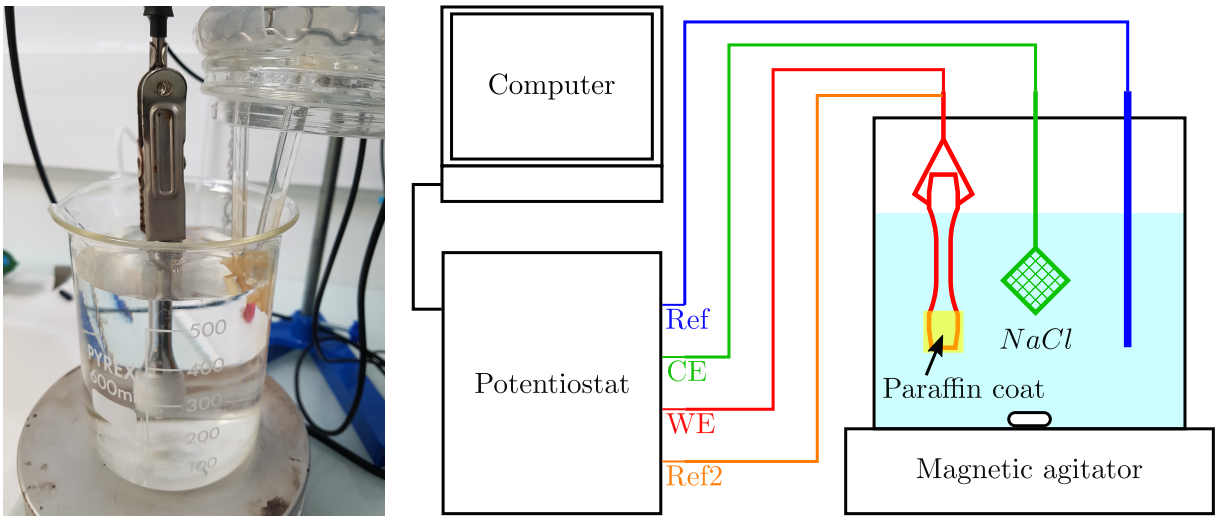

Figure 6: Polarization setup used to pre-corroded fatigue specimens.

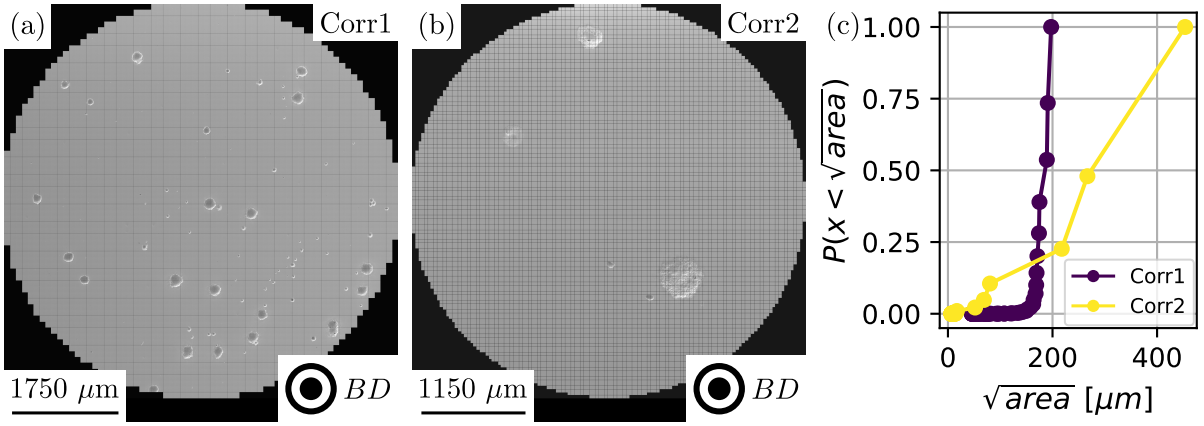

Figure 7: Two examples of different pits distributions observed with SEM microscope (a) and (b) on planar samples. Images were stitched in order to give an overview of the scanned area. Subfigure (c) gives an estimation of the cumulative distributions of defects sizes for the 50 biggest defects on the samples normalised on a surface area $S_0 = 1\ cm^2$.

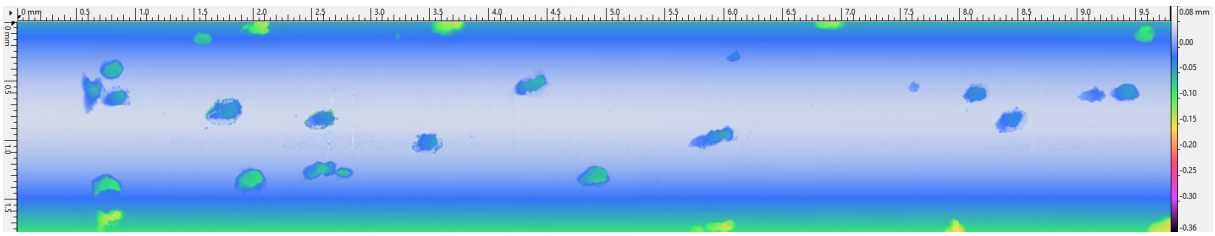

Figure 8: Example of a fatigue specimen scanned with a 3D optical microscope Bruker ContourGT-K after pre-corrosion.

3. Results and discussion

3.1. S-N curves

Figure 9 (a) shows the data for the polished batch plotted in the S-N plane. Broken specimens are represented by filled shapes and unbroken by empty ones. For comparison purposes, data taken from the litterature for L-PBF vertically built 316L are also shown : Leuders et al. [28] used machined samples, Blinn et al. [9] used machined and polished specimens and Mower and Long [36] studied net-shape samples. Loadings were also alternative and uniaxial, except for Mower and Long [36] who used rotating bending loadings. No correction was applied to the data from the literature. Our polished batch is in good agreement with the literature data, particularly with the results of Leuders et al. [28]. Mower and Long [36] data shows (as-expected) that as-built specimen surface roughness highly decrease the fatigue behaviour of the material, particularly in the high cycle fatigue (HCF) regime. Blinn et al. [9] data shows also a decreased resistance. This may be due to a higher porosity rate in their tested material (almost 1%), and probably bigger defects presence, compared to our tested material.

When comparing different surface integrities (polished, pre-corroded and with a EDM defect), see figure 9 (b), an important decrease of the fatigue resistance of the material, and a fortiori, of its fatigue strength, when surface defects are introduced can be noticed. The scatter significantly increased since various surface states were tested. The role of different nature defects in each of the given surface states is discussed in the following section.

3.2. Influence of defect type on crack initiation

3.2.1. Polished specimens

After SEM fracture surface analysis, it was observed that for the polished batch, all crack initiations took place on the surface. For only one specimen, no defect was clearly identified. Most of the fatigue cracks initiated on a LoF pore (22/23), with 17/22 2D equiaxed LoF and 5/22 elongated ones. Figure 10 shows examples of those two types of LoF. In both cases, these defects were particularly flat. Indeed, the thickness of these LoF is of the same order of magnitude as the thickness of the powder layer used during L-PBF manufacturing (30 μm). In our case, LoF defects were particularly flat and perpendicular to the loading direction. This is in good agreement with Yadollahi and Shamsaei [54] X-ray CT observations on L-PBF 17-4 PH. In this study, the authors linked this detrimental defect orientation with the fatigue strength of the material which is lower for vertically built specimens than for horizontally built ones. This trend was also observed by Le et al. [27] for L-PBF Ti-6Al-4V alloy. Thus, two observations can be made for LoF types defects : (i) their low thickness and sharp contours make their acuity relatively high (implying possible locally high stress concentration factors) and (ii) their flat aspect makes them difficult to detect, in comparison to spherical gas pores, when performing a CT scan, thus, making them potentially more dangerous for a structure's integrity.

3.2.2. Pre-corroded specimens

For pre-corroded specimens, all cracks initiated on the surface. 8/34 cracks initiated on LoF pores (1/8 on an elongated one and 7/8 on 2D equiaxed ones) and 26/34 on corrosion pits. For the LoF pores, 2/8 presented some interactions between the L-PBF defect and the pre-corrosion. However, these interactions seemed relatively weak as only some traces of corrosion were observed, even on the largest LoF observed (around 466 μm) composed by a cluster of linked LoF (figure 11). This cluster of defects was an isolated case and was the only cluster observed in this study. Some additional corrosion tests were carried out with a SEM scan before and after corrosion. Figure 12 shows 2 examples with typical SEM scans before (a) and (c) and after (b) and (d) corrosion. Dotted black lines ellipses were drawn around surface defects initially on the material samples (LoF, gas pores or polishing defects). These results seem to validate the weakness of the interactions existing between LoF and corrosion pits as the main part of the defects present before corrosion remain unchanged after anodic polarization. Corrosion pits seem to nucleate randomly on the surface and independently of the defects. Duan et al. [12] studied 316L L-PBF corrosion behaviour in different aqueous environments. They observed that gas pores could become stable pits nucleation sites in highly aggressive environments, thus, L-PBF material became more sensitive to pitting corrosion than the wrought one. The authors interpreted those results as a change of the main corrosion mechanism : for a moderate aggressiveness

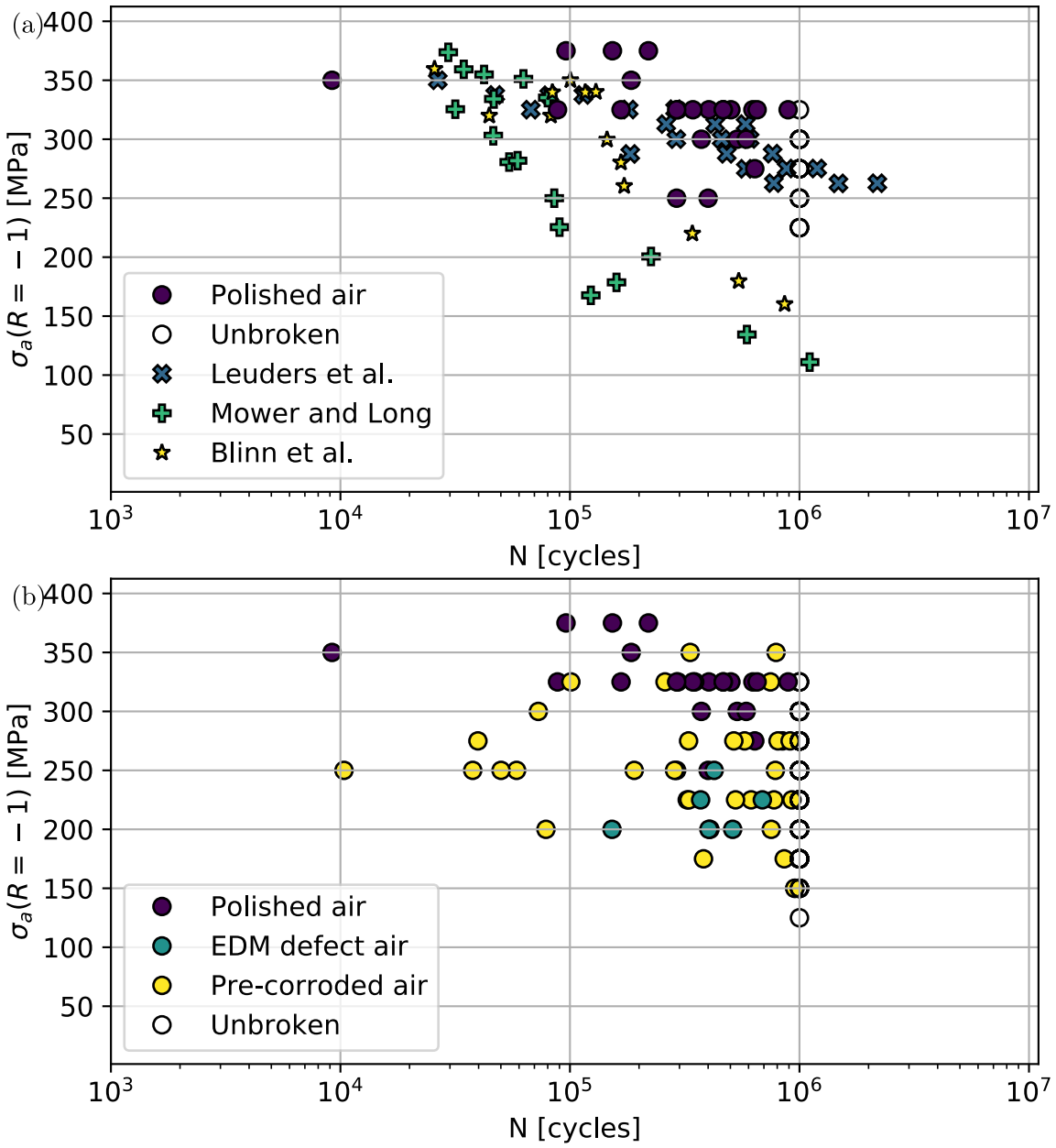

Figure 9: S-N curve at $R = -1$ ratio of (a) polished specimens compared to Leuders et al. [28], Mower and Long [36] and Blinn et al. [9] (vertical L-PBF 316L data) and (b) polished, pre-corroded and with a EDM defect fatigue specimens.

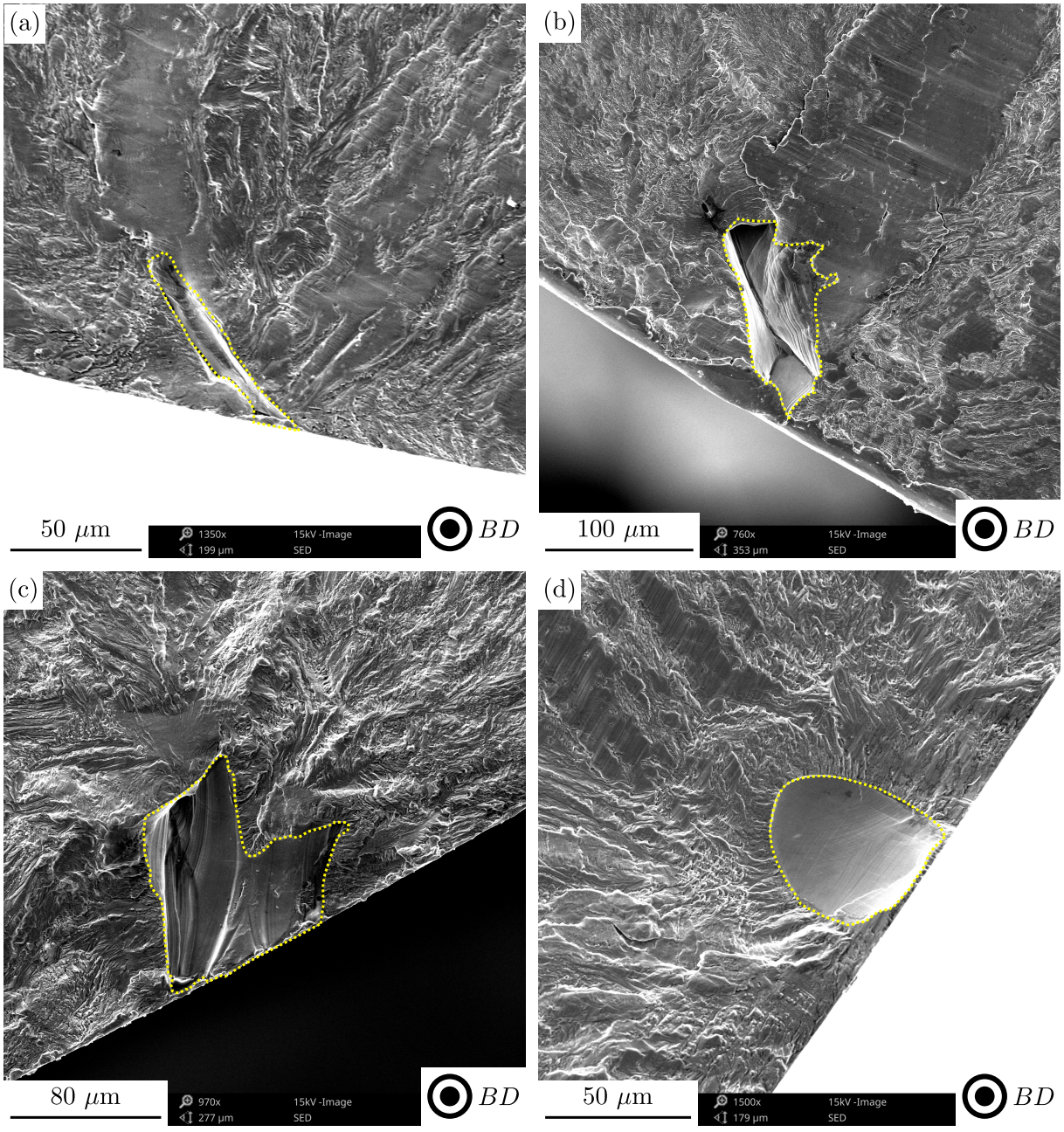

Figure 10: SEM observations of cracks initiations from (a) and (b) an elongated LoF, (c) a tortuous 2D equiaxed LoF and (d) a smooth 2D equiaxed LoF.

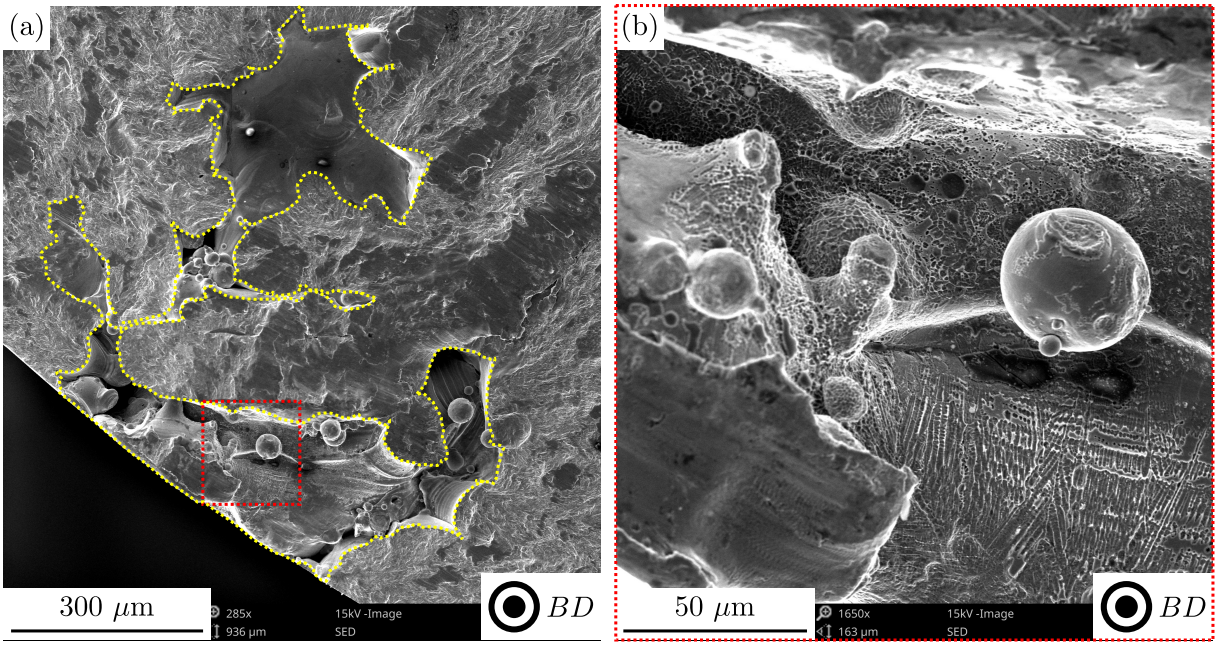

Figure 11: Crack initiation from a cluster of LoF pores. (a) is a global view of the cluster and (b) is a zoom on corrosion traces inside a LoF.

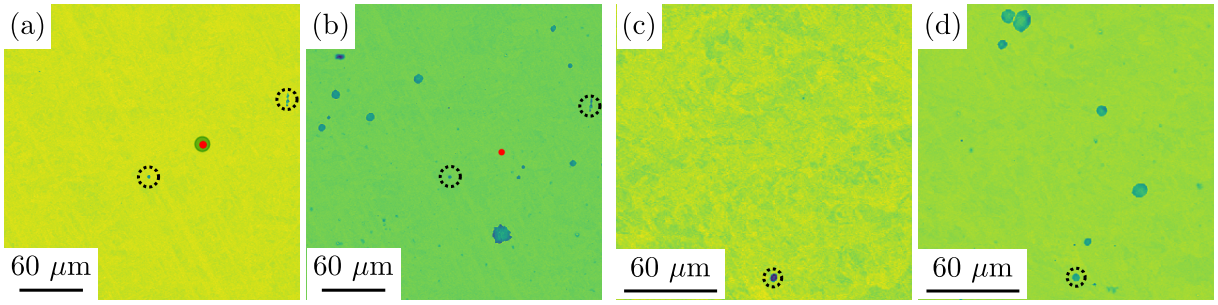

Figure 12: Surface comparison before (a) (c) and after (b) (d) corrosion on plane samples.

medium, pitting corrosion is driven by pitting nucleation (or passive film breakdown) and for a high aggressiveness medium, the main driving mechanism is the transition from metastability to stability pits. Then, the interactions between process inherent defects and pitting corrosion is related to the environment aggressiveness. Sander et al. [44] studied 316L L-PBF in a moderately aggressive solution. They focused on the effect of the material porosity on its corrosion behaviour. They observed that the free potential, the free current and the pitting potential values seemed independent of the specimens porosities. It is consistent with our observations were no correlation between the presence of a surface defect and a pit appearance could be done.

Figure 13 shows SEM images on a corrosion pit for L-PBF material (a, b, c) and L-PBF + heat-treated material (d). Some typical microstructural features inherent of the L-PBF process could be observed at different magnifications. On figure 13 (b), melt pools boundaries near the pit can be noticed. Misorientation of solidification cells can also be seen. Figure 13 (c) is an other observation at higher magnification were cells could be observed. It seems that cells walls were preferentially dissolved since cells interiors are distinguishable. Their size is around 500 nm which is in good agreement with the literature [12, 48]. In figure 13 (d) the disappearance of L-PBF features inside the corrosion pit (melt pool boundaries, cells) can be noticed, which is also in good agreement with the differences between static properties for as-built and heat-treated conditions (figure 3 (a)), due to recrystallization. This feature was also observed by Hlinka et al. [21] on L-PBF 316L. They explained these selective dissolutions as due to the chemical microsegregation existing beetwen cells interior and their boundaries, with Cr, Mo and Ni enrichment on the boundaries [48]. After

a 1050 °C heat-treatment (same temperature as used for the tensile heat-treated specimens in this study), they observed a full recrystallisation with equiaxed austenitic grains and an important grain coarsening.

Furthermore, corrosion pits morphology is irregular and could change a lot from one pit to the other. Figure 14 shows different pit examples, from the smallest (a) to the biggest (d). Pits seem to have a relatively high roughness. Indeed, the selective dissolution inside the pit increases at low scale the interior pit roughness. It could also be noticed that pits contours are irregular, with many curvature discontinuities. When focusing on the global morphology, pits seem to grow in the material depth (perpendicularly to the free surface) at the beginning of pit growth (figure 14 (a)). Then, become almost hemispherical (figure 14 (b)) before turning ellipsoidal when the pit size increases (figure 14 (c)). The larger the pit growth, the smaller the ratio between the depth and width of the pit is (figure 14 (d)). Figure 16 (d) represents the Feret ratio ($Feret_{min}/Feret_{max}$) of the critical defect population. No clear tendency could be highlighted for LoF pores in this plot, even if the data seem to show that large pores or large pores clusters are more likely 2D equiaxed than elongated in one direction. On the other hand, this figure is consistent with the pit growth mechanism previously suggested, according to which, the ratio *pit depth/pit width* decreases while the pit is growing. Ernst and Newman [15] observed this type of pit growth on 304 stainless steel and the proposed mechanism seems in good agreement with our SEM observations.

3.2.3. Specimens with an unique EDM defect

For the six specimens with EDM defects, all crack initiations took place on the introduced defect, without any observable natural defect in the EDM defect vicinity. Figure 15 shows examples of crack initiation on two of those specimens containing one hemispherical defect. These defects seem particularly smooth. The intent behind the use of the EDM technique instead of conventional machining was to limit the influence of the process on the microstructure at the immediate vicinity of the defect being created (i.e. hardening). Nevertheless, and as noted by Guerchais [18] on his study on the influence of defects and loading type on the fatigue strength of wrought 316L, the absence of residual stress measurements at the proximity of the defects does not allow to distinguish the contribution of the stress concentration due to the geometric morphology from the contribution of the process used to create the defect itself. EDM was nonetheless considered as an acceptable technique since Guerchais' results showed a 5% decrease in fatigue strength for EDM modified specimens carrying a $\varnothing 95\ \mu m$ (i.e. $\sqrt{area} \approx 60\ \mu m$) hemispherical defect in comparison to those with no added defect at all. In this study, the largest error measured between the theoretical hemispheres and the real EDM defects sizes was smaller than 2.5%. Macroscopically, the shape of these defects could be considered hemispherical. As discussed further in this paper, EDM defects were in the range of size of the critical corrosion pits. Contrarily to LoF and pits, EDM defects enabled us to fully decoupled the defect size and its morphology, as the morphology was imposed by the EDM process itself.

3.2.4. Comparative study on the morphology of the critical defects

As presented in the three latest sections, the critical defect responsible for the crack initiation in our study could be either inherent to the L-PBF process (microstructure or LoF), or due to a corrosion pit, or due to a hemispherical EDM defect. Figure 16 represents some features of the critical defects for L-PBF and pit initiations. Plot 16 (a) presents the cumulative density function $F(\sqrt{area}) = P(x < \sqrt{area})$ in function of the square root of the area $\sqrt{area}$ of our critical defects populations. Plot 16 (a) can be replot into plot 16 (b), changing the ordinate $F(\sqrt{area})$ for the reduced Gumbel variable $Y(\sqrt{area}) = -\ln(-\ln(F(\sqrt{area})))$. Gumbel cumulative density function is written in equation 2.

$$F(\sqrt{area}) = \exp\left[-\exp\left(-\frac{\sqrt{area}-\mu}{\beta}\right)\right] \tag{2}$$

with μ, the position parameter and β, the scale parameter. In plot 16 (b), equation 2 becomes the affine equation 3. The found fitted lines on our data are plotted figure 16 (b) and the affine parameters are displayed in figure 16 (c). The fitted lines describe well our data. The cluster of pores (which is a singular L-PBF defect) was not taken into account for the data fit and is found very far from the L-PBF distribution. This data point is surrounded by an empty dotted circle.

$$Y(\sqrt{area}) = \frac{\sqrt{area}-\mu}{\beta} \tag{3}$$

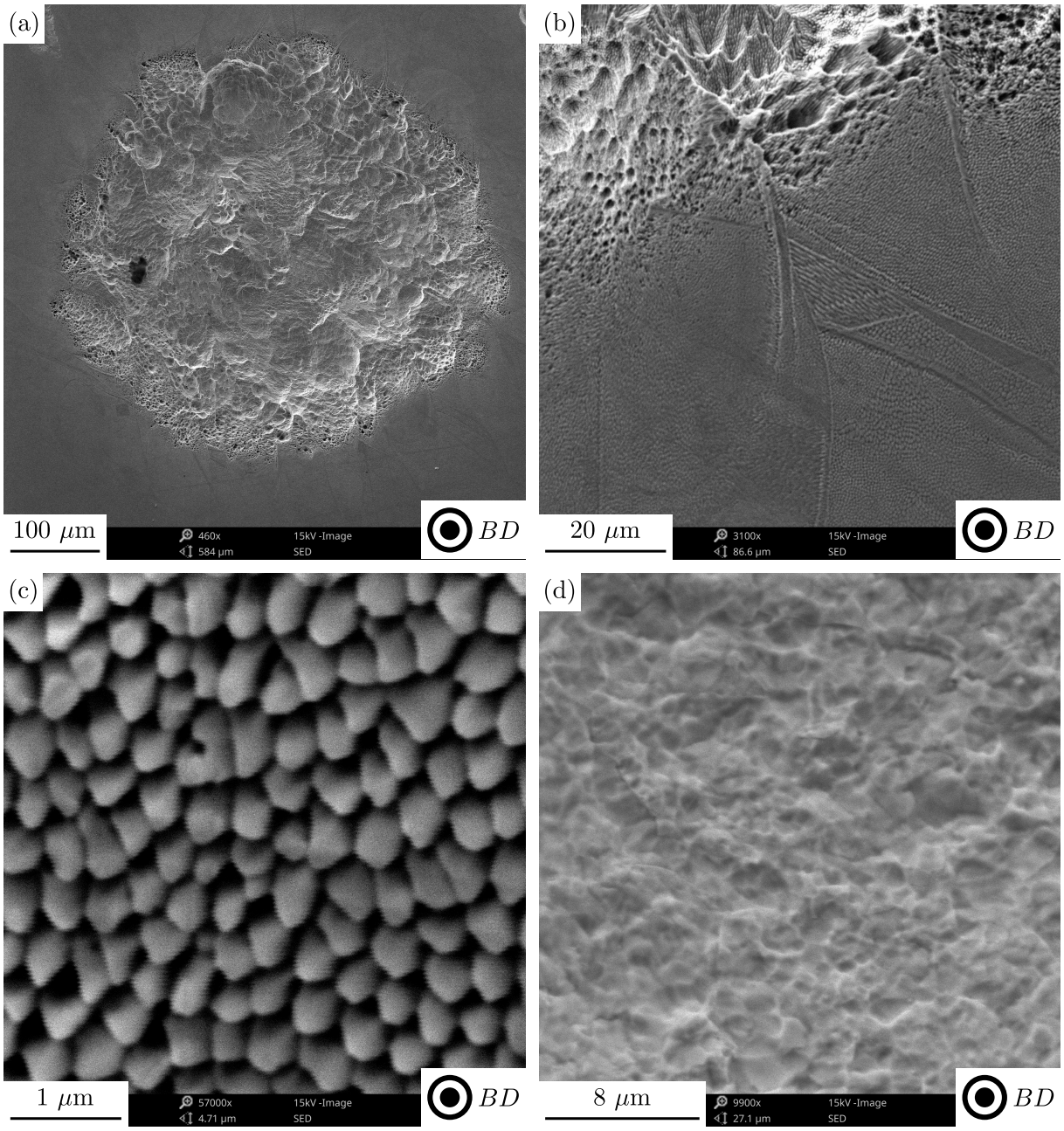

Figure 13: SEM analyses of corrosion pits for L-PBF material at different magnification (a, b, c) and L-PBF + heat-treated material at high magnification (inside the corrosion pit) (d)

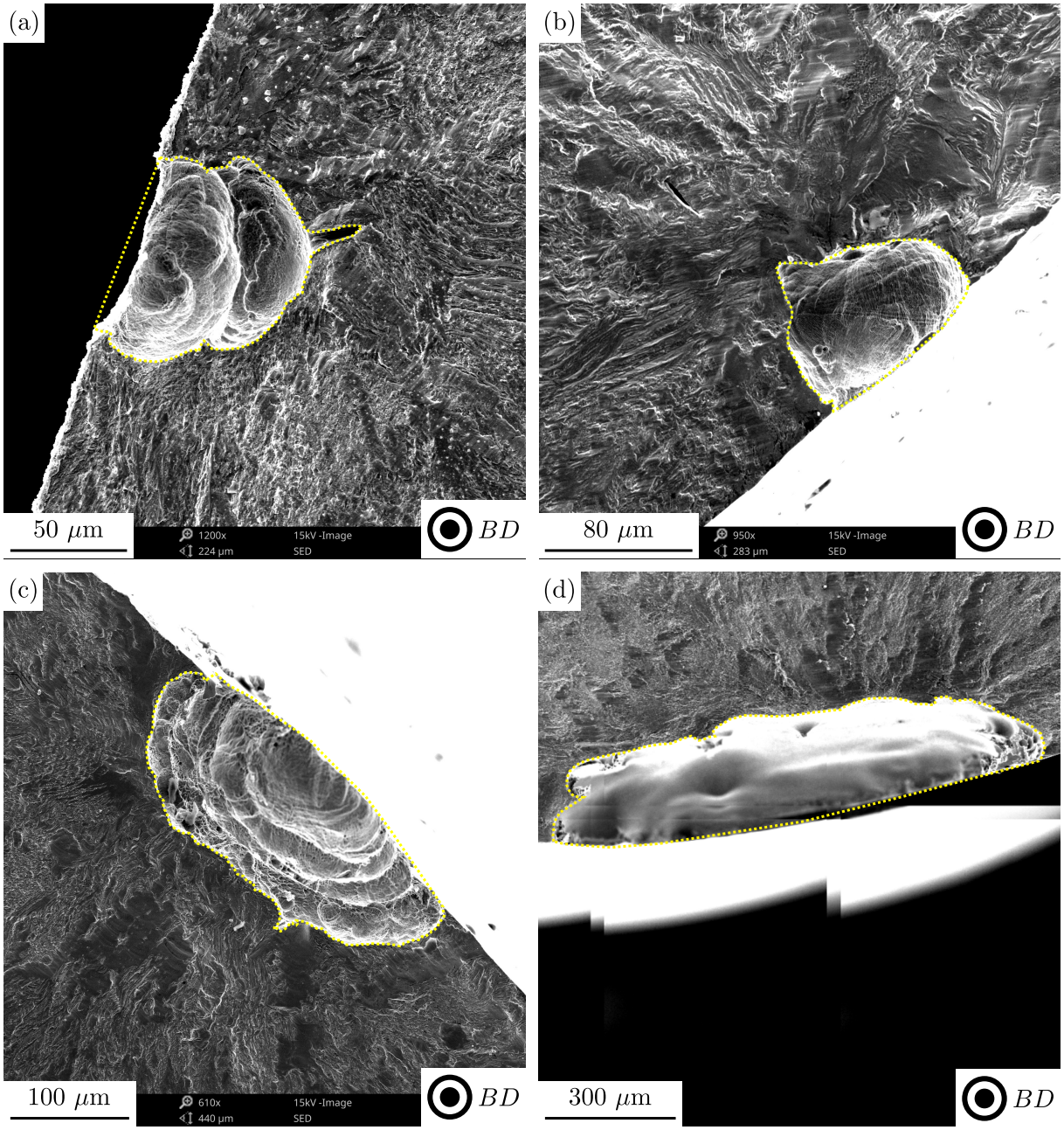

Figure 14: Different pits morphologies, from the smallest (a) to the biggest (d) in terms of $\sqrt{area}$.

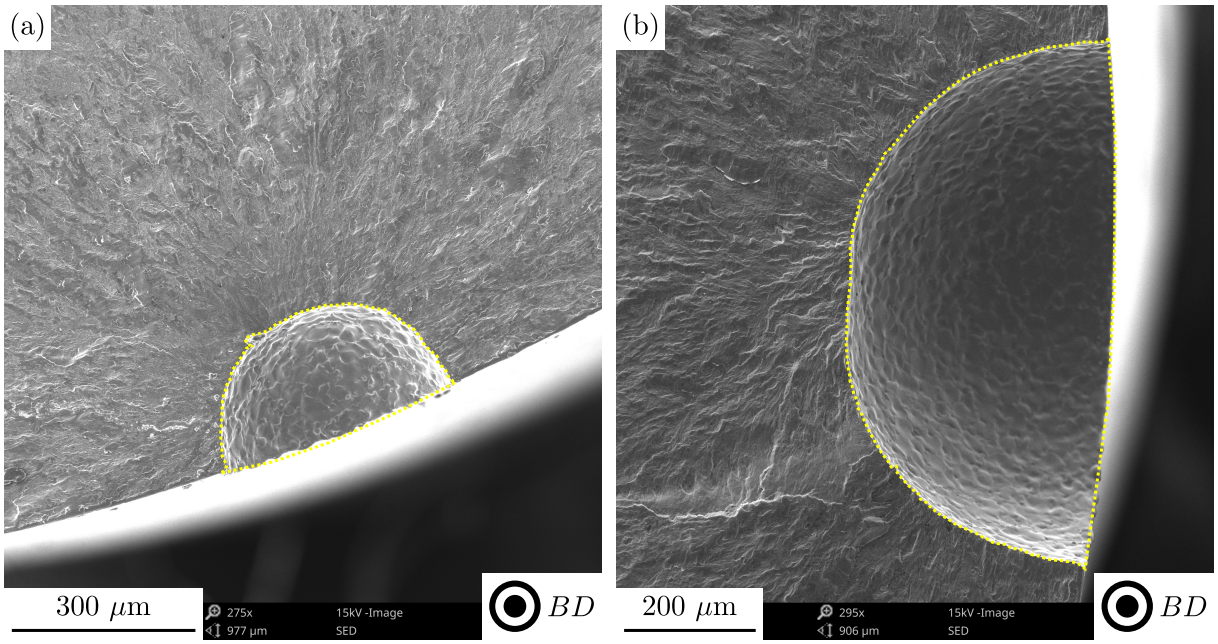

Figure 15: Examples of crack initiation from EDM hemispherical defects (a) ∅400 μm and (b) ∅800 μm.

Figure 16 (c) shows the fitted gumbel density functions $f_{gumbel}(\sqrt{area})$ for L-PBF defects and pits. Gumbel density function is described by equation 4.

$$f_{gumbel}(\sqrt{area}) = \frac{1}{\beta} \exp\left(-\frac{\sqrt{area}-\mu}{\beta}\right) \exp\left[-\exp\left(-\frac{\sqrt{area}-\mu}{\beta}\right)\right] \tag{4}$$

The position of the three EDM defects is indicated in plot 16 (c).

The critical defects size intervals for LoF $\sqrt{area} \in [1, 187]$ μm (without the cluster of LoF) and pits $\sqrt{area} \in [63, 516]$ μm covered globally a large interval in terms of defect size. An overlapping between the critical L-PBF defect population and the critical corrosion pits one can be observed. It means, that at equal size, the crack responsible of the failure could probably initiate either on a L-PBF defect or on a corrosion pit. It could mean that the size of the defect is an important parameter for the crack initiation. Indeed, in our study, the smallest pit on which crack initiation took place was of $\sqrt{area} = 63$ μm, which is very close to the median value L-PBF fitted distribution of $\sqrt{area} = 60$ μm. The following hypothesis can be stated : if the introduced defect is smaller than the largest inherent L-PBF defect, crack will initiate preferentially on the L-PBF defect and vice versa. It can be noticed as well that critical corrosion pits are bigger in terms of μ than L-PBF critical defects by a factor of 3.53. This is due to the polarization process which enable us to create large pits without limits in terms of pit size. The scale factor β is larger for the critical pits distribution than for the critical L-PBF one (with a ratio of 3.72). It underlines the stochastic nature of the pitting corrosion process, which seems even more random than the appearance of L-PBF defects during fabrication. Indeed, even at fixed electrochemical microscopical parameters (as showed figure 7 on planar samples), pits population may vary a lot. This high variability of the total pit population is well translated by the critical defect analysis. EDM defect sizes were chosen after preliminar tests on pre-corroded and polished specimens. As illustrated in figure 16 (c), the sizes were chosen in order to be highly confident of obtaining an hemispherical defect size higher than the biggest LoF in the specimen. The upper limit of EDM defect size was chosen to stay in the range of our generated critical pit size population.

Following the morphological study, the Feret ratio evolution as a function of the defect size is plotted in figure 16 (d). This factor is a good descriptor of the mesoscopic shape of the defect : it is near 1 if the defect is equiaxed and tends to 0 when the defect is elongated in one direction. Figure 16 (e) shows the evolution of the normalised defect depth (from the surface) as a function of the defect size. This normalised depth was defined as the ratio between the defect depth and the square root of the area of the defect. It gives insights

on the criticality of the defect and its orientation. Finally, figure 16 (f) highlights the evolution of the defects equivalent circularity as a function of their sizes. Our definition of the equivalent circularity is a derivation of the classic sphericity definition for a particle, where the sphericity is the ratio of the external surface area of a sphere with the same volume as the particle to the surface area of the real particle. In our case, since all our critical defects are crossing the free surface of the samples, the equivalent circularity of a defect is considered as the ratio between the perimeter of a truncated circle and the perimeter of the real defect. The chosen truncated circle must meet two conditions : (i) the area of the theoretical truncated circle should be the same as the real defect and (ii) the surface opening length of the truncated circle should be equal to the real defect one. Figure 17 illustrates the equivalent truncated circle definition, with the area of the defect S and its opening length λ. The measurement of the depth is also illustrated in figure 17 (a). The equivalent circularity here is a descriptor of the meso-roughness of the defect. Indeed, it combines the effect of the global shape of the defect with lower scale features. As shown in figure 16, no clear tendency could be observed for the lack of fusion pores. It means that LoF equiaxiality, normalised depth and equivalent circularity are independent of the defect size. These observations seem to be true for typical LoF. It can be noticed that the cluster of defects is not only singular in terms of size compared to other L-PBF critical defects, but also in terms of morphology as it is almost equiaxed, very deep for a defect of this size and highly tortuous (as it could be seen through its equivalent circularity value). For corrosion pits, our results indicate that the more the pit size increases, the more the pit is elongated in one direction. The normalised depth of a pit tends to decrease when the pit size increases. As discussed in the previous section 3.2.2, this is probably related to the pitting corrosion mechanism as proposed by Ernst and Newman [15]. The more the pit grows, the more shallow it becomes. It can be underlined that the equivalent circularity of the corrosion pits is relatively high (only two pits below 0.90). It could be explained by the low tortuosity of these defects compared to LoF and because of their near ellipsoidal shape. For the EDM hemispherical defects, the found values were near 0.50, 0.80 and 1.00 which are respectively the theoretical Feret ratio, the normalised depth and the equivalent circularity values calculated for a semicircle.

Figure 18 is a summary where the main features describing the geometrical harmfulness are shown together, including : (i) the defect size (square root of the defect area), (ii) the defect equivalent circularity (mesoscopic roughness) and (iii) the defect normalised depth. Global trends can be observed in this figure (without taking the cluster into account) :

- LoF defects and corrosion pits distinguish from one another by very different values of equivalent circularity. Although LoF defects can have a highly variable mesoscopic rugosity with equivalent circularity values going from 0.5 to 1, corrosion pits are in general highly circular (> 0.85). Corrosion pits can thus be considered as having a smoother contour.
- No critical defect over the size of 200 μm was a LoF. It is unknown if this corresponds to the absence of LoF defects larger than 200 μm or to a factor of "criticality" specific to larger corrosion pits (i.e. $>$ 200 μm).
- The larger the defect is, the smaller the normalised depth is.

As a conclusion, for the critical defects observed, the more the size increase, the less these defects seems critical in terms of geometry. There is an exception for EDM defects for which the criticality of their geometry remains constant for all sizes. Further in this article, the term of "geometrical criticality" of a defect refers to a parameter which increases the deeper the defect is, and the less circular (i.e. the more tortuous) it is. The following sections will discussed about the defect criticality regarding the experimental fatigue strength of the tested specimens.

3.3. Effect of defects on the fatigue resistance

3.3.1. Influence of the defect size

In order to link the size of the defect responsible of the fatigue crack initiation and the stress level at fracture, a Kitagawa-Takahashi diagram is plotted figure 19. This representation shows our raw data results (i.e. at nominal stress amplitude). Only results for which the defect contour could be confidently defined were plotted. Empty markers represent steps where the sample did not break at the end of the step (10^6 cycles), filled ones were used when the sample broke during the current step (less than 10^6 cycles). The color indicates the belonging of the sample to one of the batches, either polished, pre-corroded or EDM,

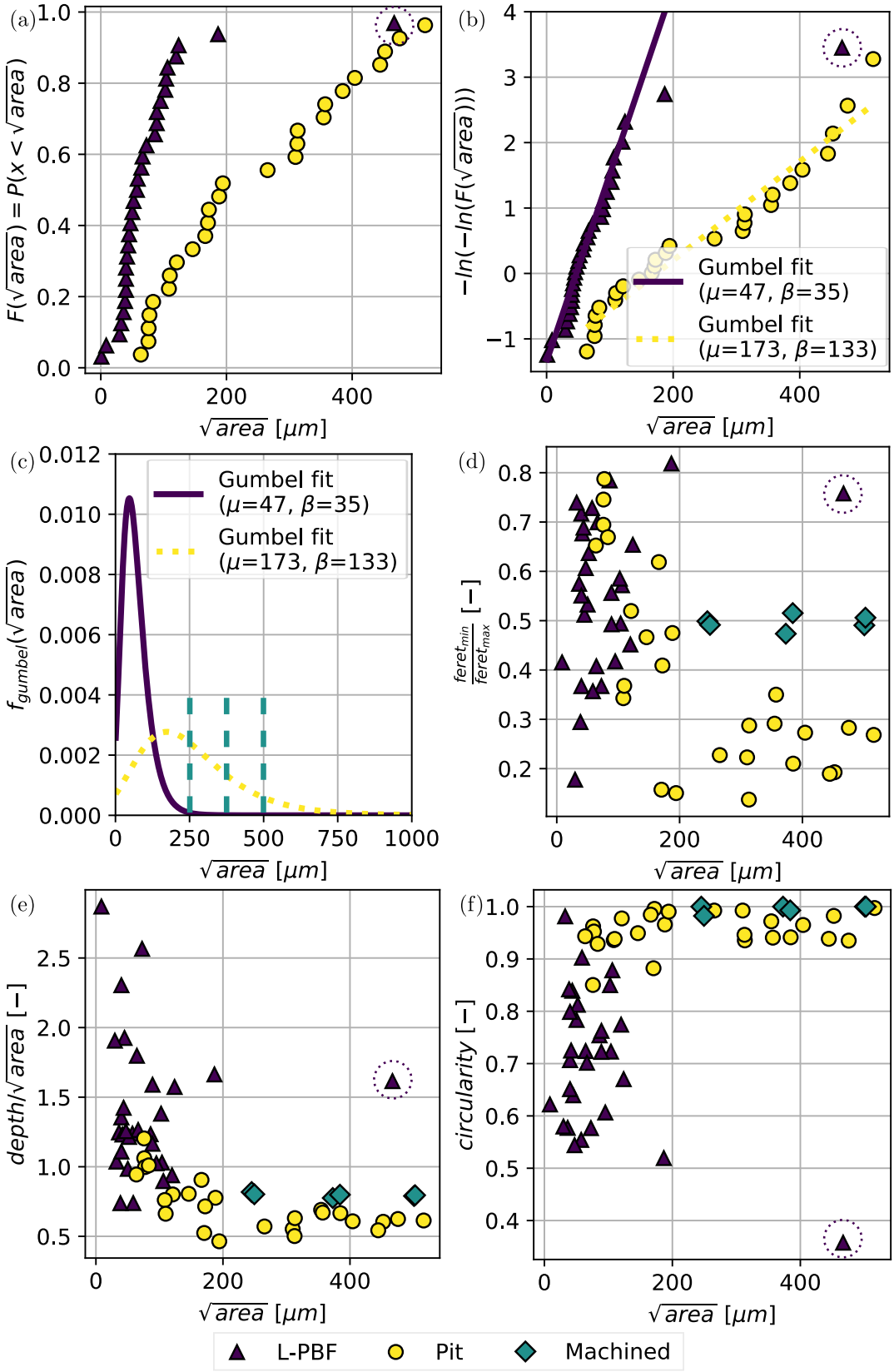

Figure 16: Critical defect population in terms of $\sqrt{area}$, with (a) the cumulative density function F, (b) the fit of Gumbels laws on our data per defects types, (c) the fitted density functions, (d) the Feret ratio, (e) the normalised depth and (f) the equivalent circularity.

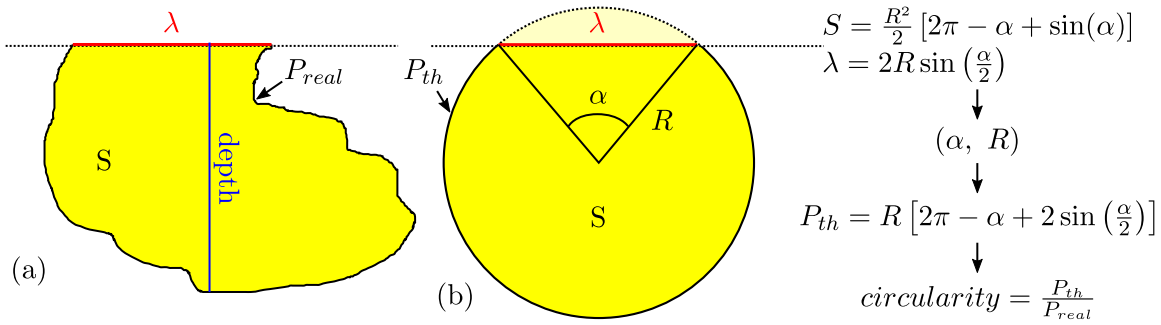

Figure 17: Defect theoretical equivalent truncated circle definition, with (a) the real defect and (b) the found equivalent truncated circle.

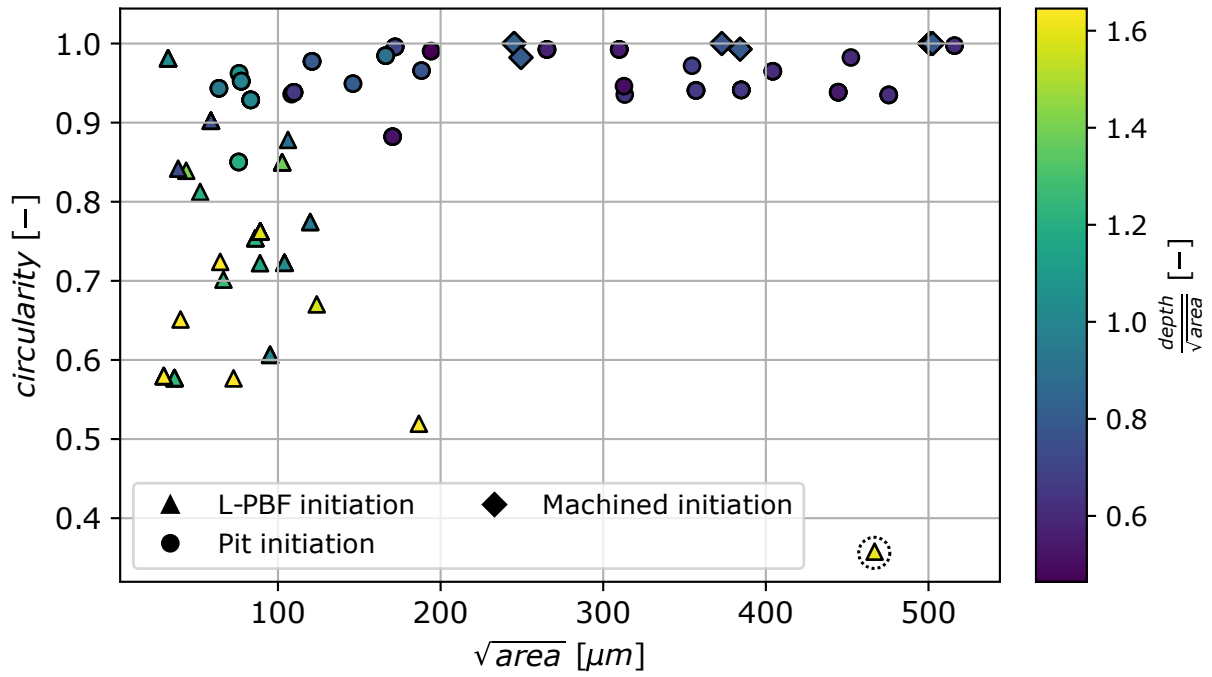

Figure 18: Critical defect equivalent circularity as a function of the defect size $\sqrt{area}$ and its normalised depth (in colorbar).

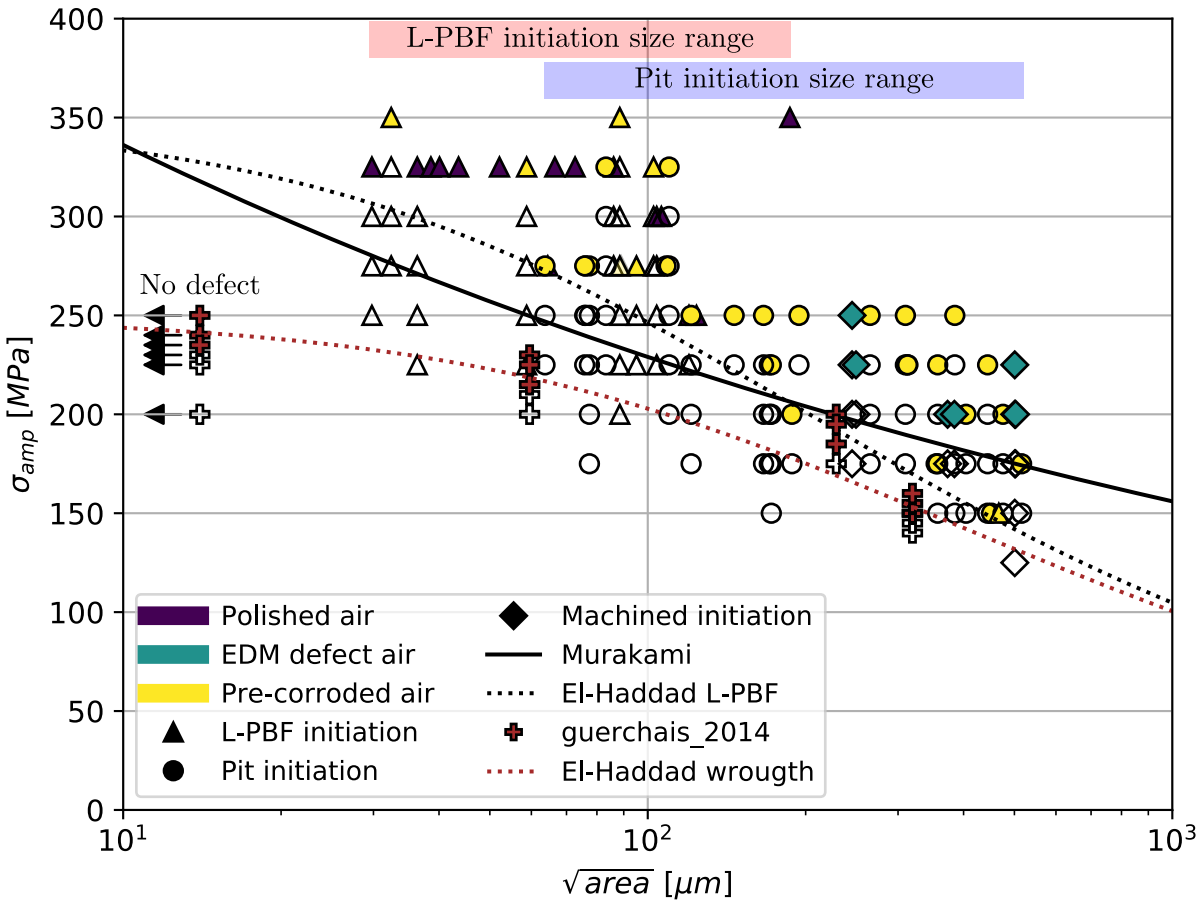

Figure 19: Kitagawa-Takahashi diagram of raw data, from our study and Guerchais [18].

and its marker shape the nature of the defect where the crack initiation took place. Samples for which fracture occurred during the first step and below 10^5 cycles are represented in transparency. In our study, the data labelled as "Machined initiation" refers to electric discharge machined defects. Murakami (equation 5) and El-Haddad (equation 6) models are also represented on the figure, with plain and dotted black lines respectively.

$$\sigma_{D,a} = \frac{1.43(H_v + 120)}{\sqrt{area}^{1/6}} \tag{5}$$

$$\begin{cases} \sigma_{D,a} = \frac{\Delta K_{th}}{0.65 \times \left(\pi(\sqrt{area} + \sqrt{area_0})\right)^{1/2}} \\ \sqrt{area_0} = \frac{1}{\pi} \times \left(\frac{\Delta K_{th}}{0.65 \times \sigma_{D0,a}}\right)^2 \end{cases} \tag{6}$$

In this study, $\Delta K_{th} = 4\ MPa\sqrt{m}$ and $\sigma_{D0,a} = 350\ MPa$ were taken from the literature [37, 41]. The value of the Vickers hardness was measured on our material. Ten indents were realised, revealing a H_{v20} hardness of 225, which was the value used for the plots. Some data taken from a study of Guerchais [18] on wrougth 316L is also plotted (red '+') on figure 19 for comparison purposes. In Guerchais' work, defects were created by machining smooth hemispherical defects on the specimens using the electric discharge process. Another El-Haddad fitting was drawn in dotted red line for the wrougth material with $\Delta K_{th} = 4\ MPa\sqrt{m}$ and $\sigma_{D0,a} = 250\ MPa$. For our data, an important scatter (around 100 MPa for a given defect size) can be noticed. Each test being conducted till fracture, the number of cycles of the final step is different from one test to the other. In consequence, a damage correction was applied. The full procedure is described in the following paragraphs.

Figure 20 shows the defect size as a function of the number of cycles to fracture for the ultimate step of different specimens at constant stress amplitude (200, 225, 250 and 325 MPa). Globally, no trends could be

identified. However, most of the samples were observed to break between 10^4 and 10^6 cycles (only one below, at 9194 cycles) during their ultimate loading step. It means that for most of the specimens, the fracture occurred in the HCF regime. The step by step methods with large number of cycles per steps (10^6) seem to be an efficient way to approach the fatigue limit without overshooting its value excessively (less than 25 MPa). Nevertheless, as each specimen was submitted to a different loading history, the Basquin's model (equation 7) and the Miner cumulative damage law (equation 8) were used to homogenize our results.

$$N_f = A\sigma_{amp}^{-b} \tag{7}$$

$$D = \sum_{i=1}^{k} \frac{n_i}{N_{fi}} \tag{8}$$

with N_f as the number of cycles to failure at σ_{amp} using Basquin's model, k as the last step number, n_i as the number of cycles at step i, N_{fi} as the theorical number of cycles to failure at step i, A as a constant for each specimen and $b = 8$. The value of b was chosen in accordance with the S-N behaviour of the polished batch. Using the equivalence of damage at failure ($D = 1$), the expression 9 can be written.

$$\frac{N_{ref}}{A\sigma_{corr}^{-b}} = \sum_{i=1}^{k} \frac{n_i}{A\sigma_i^{-b}} \tag{9}$$

with $N_{ref} = 10^6$ cycles, the number of cycles to failure at the corrected stress amplitude σ_{corr}. Thus, the equation 9 can be rewritten as equation 10 to calculate the corrected stress amplitude.

$$\sigma_{corr} = \left[\frac{1}{N_{ref}} \sum_{i=1}^{k} n_i \sigma_i^b \right]^{1/b} \tag{10}$$

Figure 21 (a) shows our raw data with the stress amplitude as a function of the defect size. A colorbar is used to represent the logarithmic value of the number of cycles to fracture on the ultimate step ($N = 10^6$ if the fatigue specimen is unbroken, represented by the empty markers). As discussed before, no clear trend could be observed in terms of number of cycles to failure. Figure 21 (b) shows our corrected data applying equation 10. Guerchais' data [18] were also corrected using the same equation and plotted for comparison purposes. It can be highlighted that only one specimen (in transparency) broke below 10^5 cycles during its first loading step (almost 40.000 cycles). The second smaller number of cycles to fracture at first step observed was almost 167.000 cycles. Because of the relatively low number of cycles observed for the specimen in transparency, it was not taken into account in the following analyses.

First of all, a good correlation between the parameter $\sqrt{area}$ and the fatigue strength at 10^6 cycles can be pointed out, for our raw and corrected data (respectively in figures 19 and 21 (b)). This correlation seems to be independent of the batch, but also of the defect type (LoF, pit or machined), which was unexpected considering the numerous morphological differences between LoF pores, corrosion pits and hemispherical machined defects. However, first analyses of our results in figures 16 (a), (b) and (c) were already pointing in this direction since the smallest critical pit was almost equal to the median value of the L-PBF size distribution. Both models (Murakami and El-Haddad) gave a good fatigue limit prediction for the tested material, in a rather conservative way. As shown in the diagrams, there is a zone where L-PBF pores and corrosion pits critical defects are merged. This increases the confidence in the correlation between the defect size and the fatigue strength, as two defects of the same size (in terms of $\sqrt{area}$) seem to be equally harmful regarding the fatigue limit. Even if the defect size seems to be the first order parameter which characterizes the criticality of a defect, the dispersion of our data indicates that other parameters may have a role on the fatigue strength of the specimens. The comparison of our raw data (figure 19) and corrected data (figure 21 (b)) doesn't show any benefits in terms of scatter of the correction given by equation 10. It could mean that the number of cycles to fracture has no obvious effect for a number of cycles to fracture between 10^4 and 10^6 cycles, as shown in figure 20 and figure 21 (a). The following sections will treat about the possible second order parameters which could be at the origin of this important scatter.

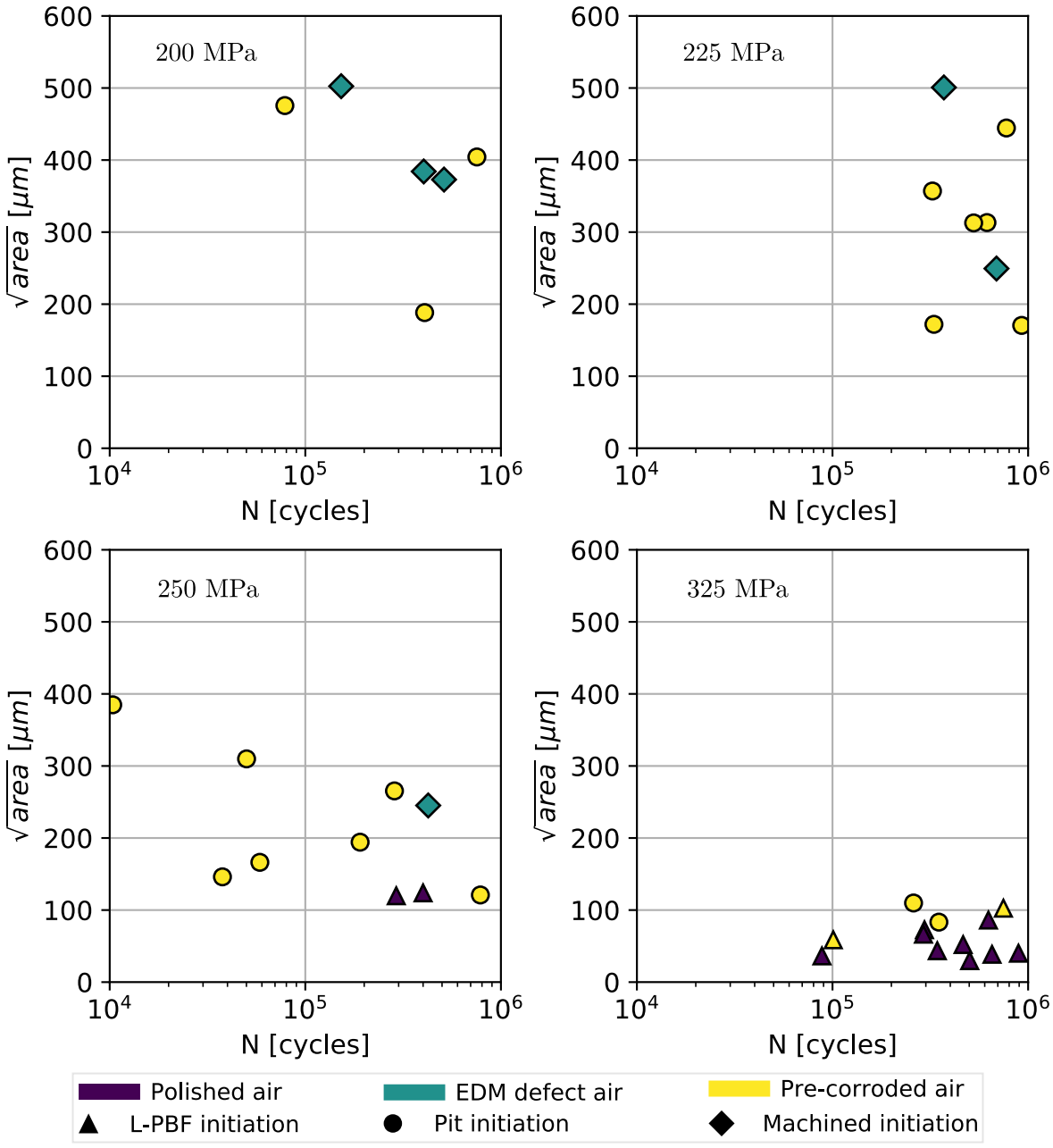

Figure 20: Plot of the number of cycles to fracture (N) and the defect size ($\sqrt{area}$) at constant stresses.

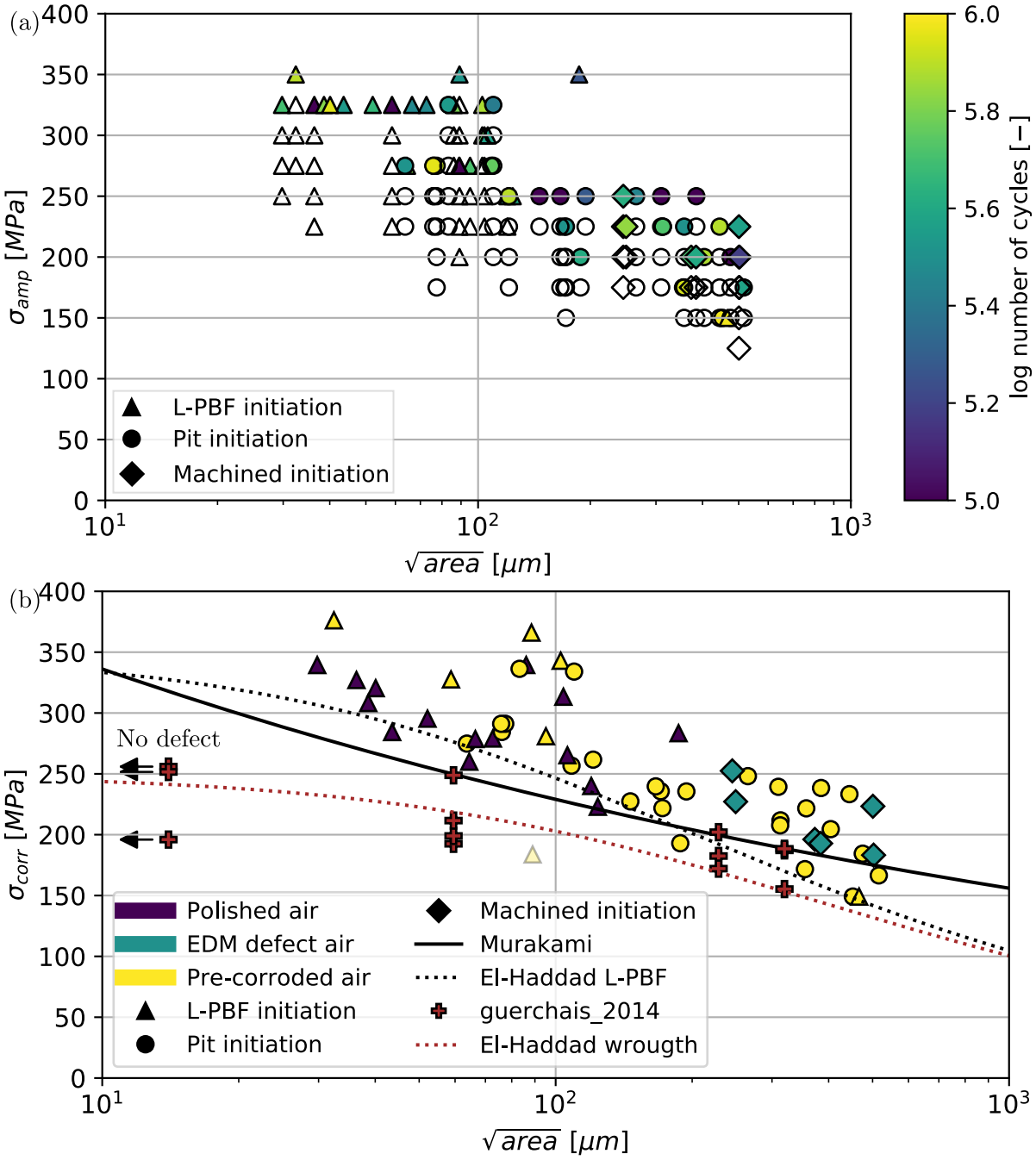

Figure 21: Kitagawa diagrams of (a) our raw data with the number of cycles to fracture in the colorbar and (b) the corrected data including results from Guerchais [18].

3.3.2. Influence of the defect morphology

As discussed in section 3.2, various types of critical defects were observed, from different sources and with very different morphologies. Figure 22 represents the corrected fatigue strength as a function of the defect size which was pointed out to be the first order parameter driving the criticality. Colorbars show (a) the normalised depth of the defect and (b) the defect equivalent circularity. The only trend observable is the decrease of the defects presumed geometrical harmfulness when their sizes increase as shown in figure 18 and discussed in this paper earlier.

Another way to observe more precisely the effect of the defect morphology is to observe defects case by case. Figures 23, 24, 25 and 26 illustrate four case by case studies at different scales of defects sizes. For each of these figures, a radar plot showing different defects features and the corrected experimental fatigue strength is plotted. Two or three defects are compared in each graph. The associated fracture surface SEM observations are also shown.

Figure 23 shows a case where the fatigue strength of the specimens is almost identical (between 275 and 280 MPa) and their critical defects sizes (in terms of $\sqrt{area}$) are quite small and close (between 60 and 75 μm). On the other hand, their equivalent circularity, their normalised depth and their Feret ratio are very different from another. For example, the comparison between the critical defects of specimens "A3" and "F4" shows very different geometrical aspects. "A3" shows a tortuous and deep defect oriented in the specimen depth whereas "F4" is a near hemispherical corrosion pit rather shallow. The geometrical criticality of "A3" seems higher than for "F4", however, there experimental corrected fatigue stresses are almost equal. It means that in this case, the size of the defect seems to be the only driving parameter in terms of fatigue strength. As it will be shown next, this is not always the case.

Figure 24 displays a good counter example when the $\sqrt{area}$ parameter doesn't seem to be sufficient to determine the criticality of defects. The first proposed comparison is between the very circular and smooth pit "A8" and the highly tortuous and sharp LoF "F5". These two defects have very different fatigue strengths ("A8" : 193 MPa and "F5" : 283 MPa) while their sizes are almost the same ("A8" : 188 μm and "F5" : 187 μm). This result is very counter-intuitive since these two defects have equivalent sizes and "A8" seems (from a mesoscopic point of view) mechanically less detrimental than "F5", but is experimentally highly more detrimental. "C6" and "F5" can also be discussed about. This time, defects have the same fatigue strength ("C6" : 284 MPa and "F5" : 283 MPa) but different sizes ("C6" : 76 μm and "F5" : 187 μm). The corrosion pit "C6" is more circular and less deep than the LoF "F5", then, an higher fatigue strength for "C6" than for "F5" could have been expected. Still, our experimental results prove this hypothesis wrong. This case study indicates that in some cases, the size of the defect is not the only driving force for crack initiation since two defects with the same sizes could have very different fatigue strength (90 MPa between "A8" and "F5"), or inversely two defects with the same fatigue strength could have different defect sizes (111 μm between "C6" and "F5"). In both cases, other morphological features did not help to explain these contradictions.

Figure 25 presents the third comparison. In this case, defects are almost equal in terms of sizes and have different natures. A comparison of the elongated corrosion pit "B7" with the hemispherical EDM defect "J3" can also be done. The size of these two defects are close ("B7" : 452 μm and "J3" : 501 μm) but their fatigue strengths are very different ("B7" : 149 MPa and "J3" : 223 MPa). The equivalent circularity of these two defects are almost equal, meaning that their tortuosity are relatively small (at mesoscale). The "B7" normalised depth is 23% smaller than the one for "J3". According to these features, it could be guessed that those defects should have almost equal fatigue strengths, or even a higher one for "B7". The comparison between "B7" and "E0" is also very interesting. These two defects have almost the same size ("B7" : 452 μm and "E0" : 467 μm) but also the same fatigue strength ("B7" : 149 MPa and "E0" : 149 MPa). In this case, the size of the defect appears to be the perfect descriptor of the defect criticality. Indeed, the other morphological features are very different : the LoF "E0" is very tortuous but also very deep whereas the corrosion pit "B7" is mesoscopicaly smooth and shallow. Looking on the whole case, "B7" seems mechanically closer to "J3" than to "E0", but, experimental results indicate the opposite.

The last case studied is shown in figure 26. In this case, the hemispherical EDM defect "J6" and the shallow corrosion pit "F2" have almost the same size ("J6" : 384 μm and "F2" : 385 μm). Like in the previous

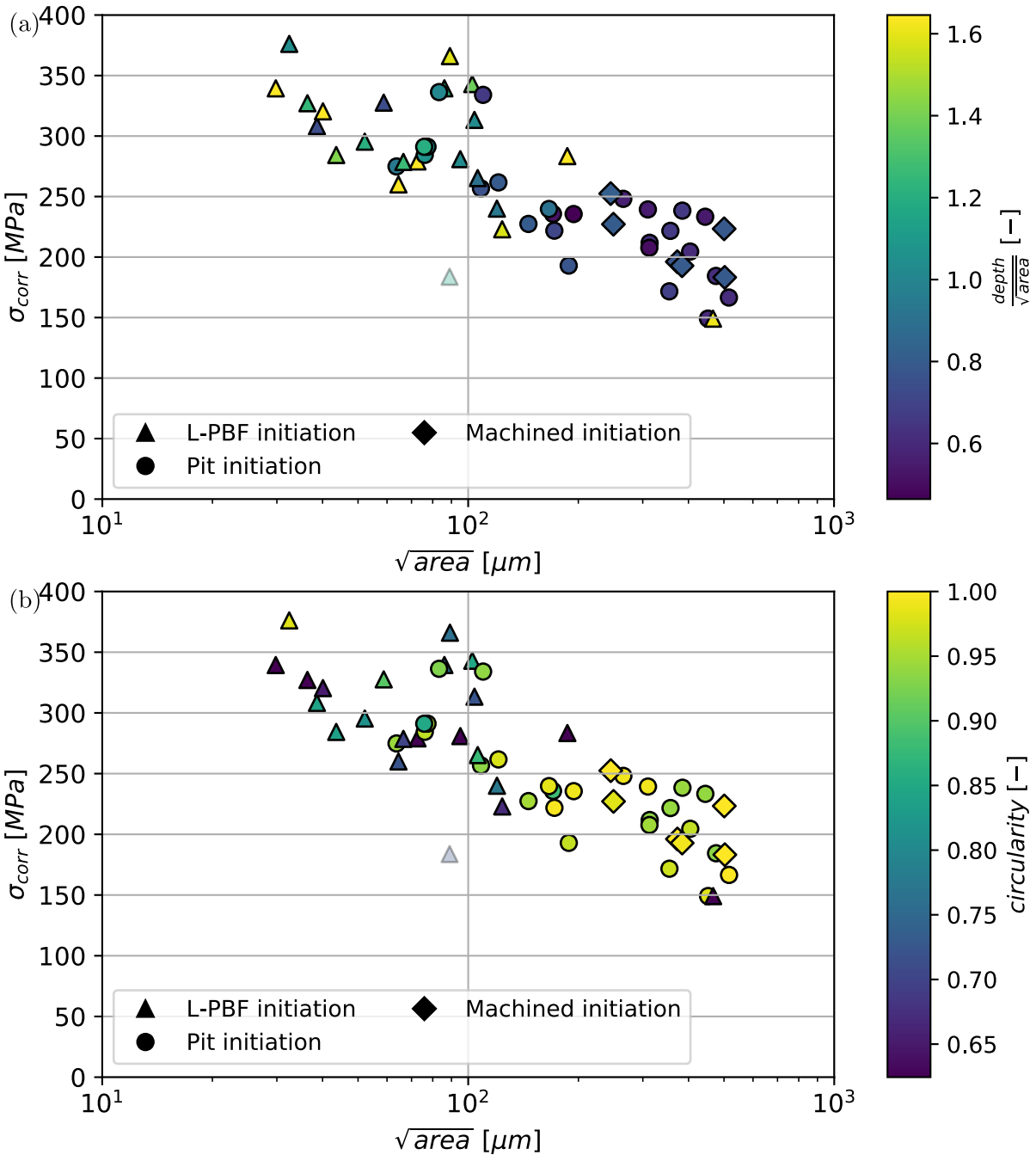

Figure 22: Kitagawa diagrams of the corrected data with (a) the normalised depth and (b) the equivalent circularity as colorbars.

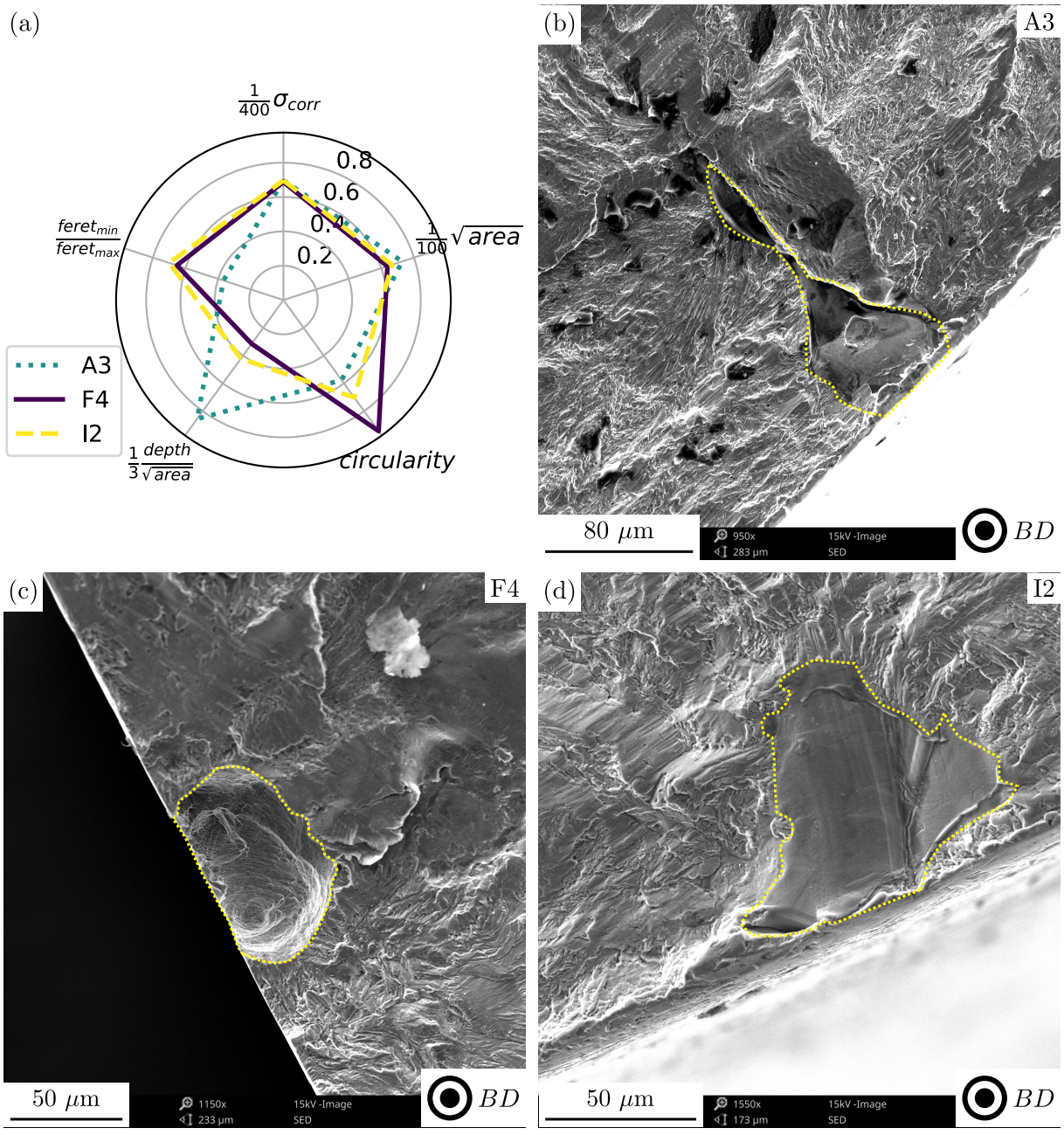

Figure 23: Comparison of three different defects of same size and criticality but with different morphological features.

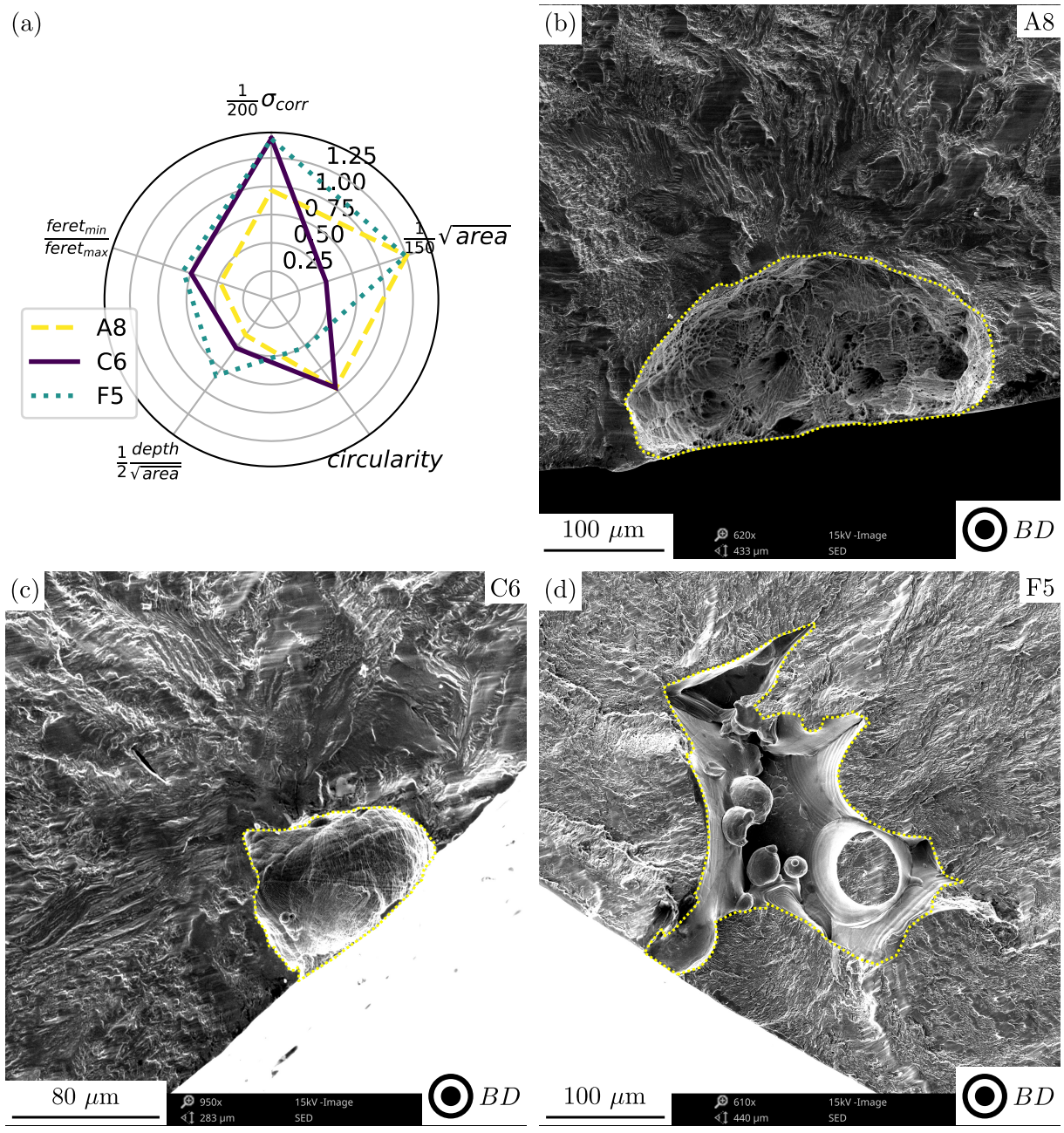

Figure 24: Comparison of three different defects with various morphological features and criticalities.

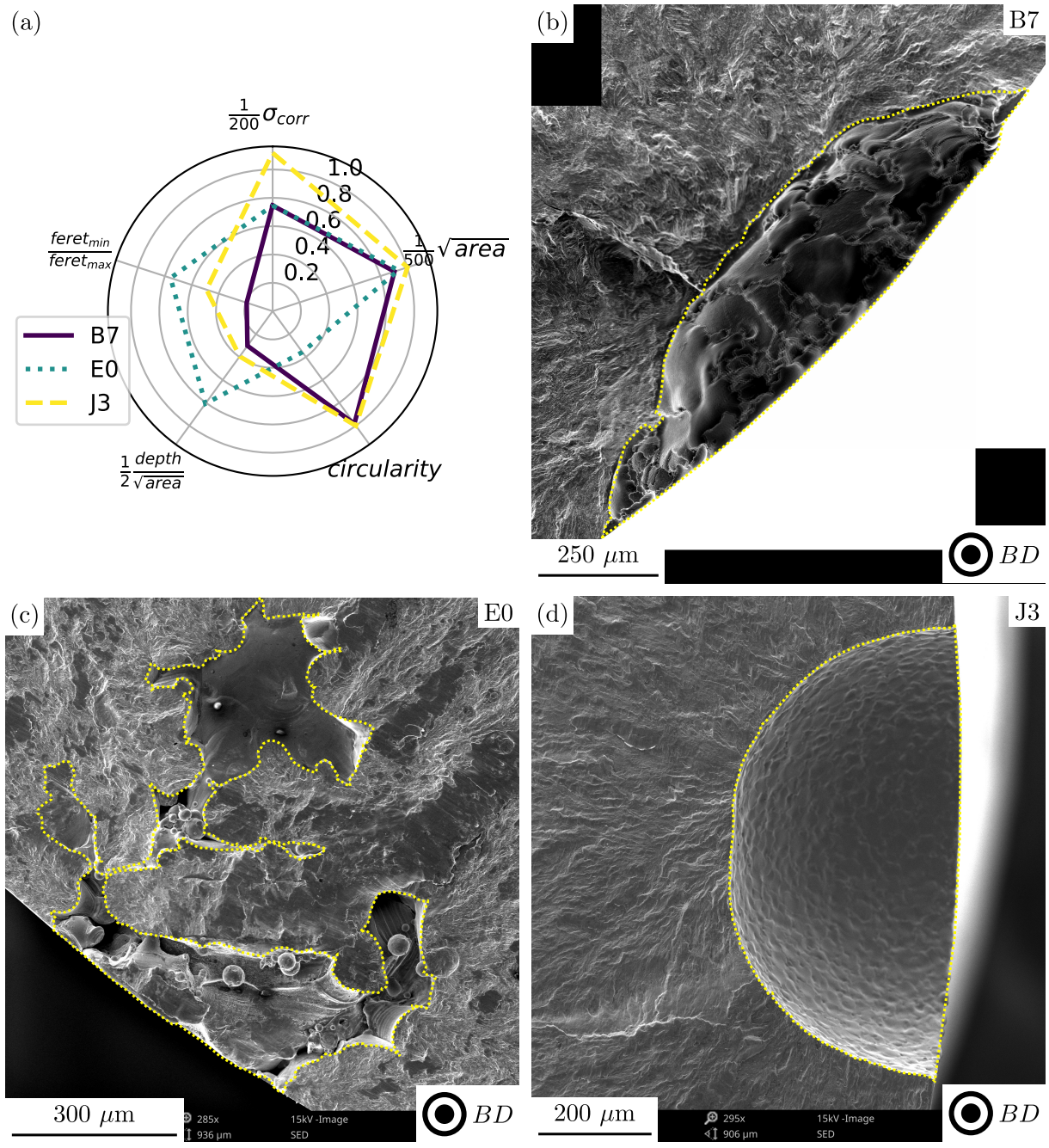

Figure 25: Comparison of three different defects with various morphological features and criticalities.

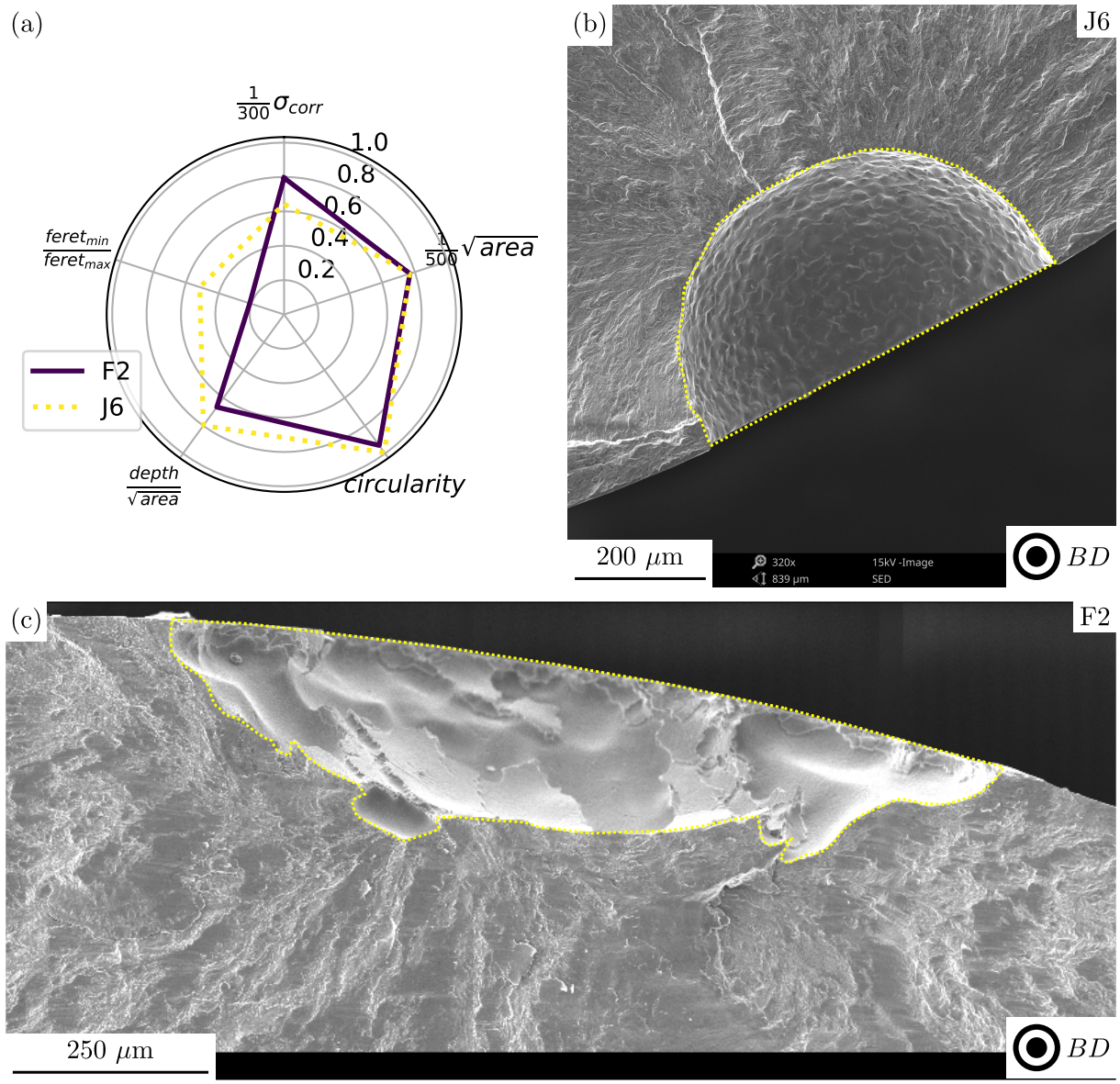

Figure 26: Comparison of two different defects with various different criticalities but almost equal defect sizes.

case (figure 25), the equivalent circularity and the normalised depth of the corrosion pit are a bit smaller than for the hemispherical defect (respectively 5% and 17% smaller). With exactly the same background as the previous case, this time the corrosion pit is less critical than the EDM defect according to our experimental results ("J6" : 193 MPa and "F2" : 238 MPa). Schönbauer and Mayer [46] studied the effect of various types of defects on the fatigue strength on martensitic stainless steels (including corrosion pits). They observed an important effect of the defect geometry on its fatigue strength, particularly for large defects. The main geometrical parameter explaining these differences was the notch root radius ρ of the defect according to the authors. The smaller this notch radius is, the more harmful the defect is. They defined the root radius of corrosion pits as $\rho << 10\ \mu m$. The EDM root radius is equal to the radius of the hemisphere so $\rho = 300\ \mu m$ for "J6". This criterion indicates that a corrosion pit should be a lot more detrimental than an EDM defect. Again, this morphological consideration is also contradictory with the empirical results in this case.

Discussions in this section underlined that a mesoscopic analysis of defects morphologies was insufficient to describe the harmfulness of a defect. The defect size remains the only consistent parameter to model a defect criticality for fatigue strength. The scatter of the data does not seems to be linked to the defects

morphologies. The following section will discuss about the effect of the microstructure.

3.3.3. Influence of the microstructure

Comparing our results against Guerchais' data [18] on figures 19 and 21 (b), it could be noticed that the found fatigue strength seemed greater for the studied 316L L-PBF material than for the wrougth one, in particular, for small defects. This gap seems to decrease as the defect size increases. The El-Haddad fits proposed for L-PBF material (our data) and the wrougth one (Guerchais [18] ones) represent this trend well. This observation may be explained by the fact that the microstructure of the material could impact the fatigue crack initiation for small defects. The larger the critical defect is, the smaller the influence of the microstructure would be. Indeed, the fine microstructure resulting from the L-PBF process might not only provide high static properties to the material, but also, an improved fatigue strength when defects near the surface are sufficiently small.

Andreau [3] observed the intrinsic matrix fatigue strength (i.e. microstructure crack initiation) of L-PBF 316L and compared its data with Guerchais' results [18]. He observed an increase of the fatigue strength of the L-PBF material of about 1.35 times, founding a fatigue limit almost at the material ultimate tensile strength. When the defect size increases, Andreau [3] observed a smaller decrease of the fatigue strength for the wrougth 316L [18] than for the L-PBF one, with a fatigue strength becoming higher for the wrougth material when the defect size $\sqrt{area} > 50\ \mu m$. However, Andreau [3] used $R = 0.1$ load ratio whereas Guerchais [18] used $R = -1$. The comparison was then based on an extrapolation based on Gerber's law, which did not take local plasticity effects into account. Real maximal stresses were higher in Andreau [3] case, thus, the comparison was unfavorable for the L-PBF material. These observations are consistent with our results.

On the same line of thought of linking microstructure and fatigue strength for an additively manufactured alloy, Shamir et al. [47] studied the role of the microstructure in the critical defect neighbourhood on the HCF behaviour for a L-PBF Ti-6Al-4V alloy. They found that the defect size was not the only driving parameter, but the defect location (i.e. distance from the surface) and the variations of the crystallographic orientation and microstructure nearby were also important to predict fatigue strength. At a given defect size and location, they observed that the scatter in fatigue life could be partially explained by the local variations of cristallographic orientation of α laths in the defect vicinity, but also by the size of these α laths.

Nevertheless, if the microstructure effect on the fatigue crack initiation decreases when de defect size increases, a decrease in our data scatter for large defects if no other effect counter-balances it should be observed. However, the scatter seems to be constant for all defects sizes, which may discard the hypothesis of considering the microstructure as the only origin of the observed scatter.

4. Conclusion

The present study gave us elements to answer the questions raised in the introduction :

- Corrosion pits affect the fatigue strength of the material. The observed decrease was not constant since it depends on the pit population (particularly the biggest pits) generated by the corrosion process. In this study, the fatigue limit of specimens without corrosion is around 325 MPa. This value is decreased by more than a half in the most critical case after pre-corrosion.
- Interactions between L-PBF inherent defects and pitting corrosion seem scarce in neutral saline solution. No corrosion pit initiation was observed on L-PBF pores, and only traces of corrosion on those defects could be observed in some cases.
- After fatigue tests on various surface states (polished, pre-corroded and with EDM defects), Kitagawa-Takahashi diagrams highlighted the competition between defects of different natures. The smallest pit observed where a crack initiation took place measured around 60 μm. Below this value, all cracks initiated on a LoF defect (excepted one for which the origin was unclear).

- Macroscopically, the $\sqrt{area}$ of the defect seems to be the main driving force for crack initiation. The defect type does not seem to play a role as two defects with the same size were observed to be in general as harmful. The dispersion of our data (around 100 MPa for a given size) suggested that other parameters need further consideration (e.g. microstructure on the vicinity of the critical defect).
- Some 2D morphological features of the critical defect measured on the fracture surface were analysed. For a fixed defect size, none of them could explain the difference of criticality between defects.
- The comparison between our data and data of wrougth 316L from Guerchais' study [18] showed that : (i) the L-PBF 316L used in this study had better HCF properties than a wrought one and (ii) the larger the critical defect, the lower the difference between L-PBF and wrought fatigue strengths was.

The scatter of our data remains unexplained. Further work focusing on 3D defect morphologies features (which could not be analysed from SEM data) will be conducted using a finite element simulation approach. Some possibly important features such as the defect acuity may be taken into account. The results will be discussed in an other study. The critical defect size interval in this study covered two orders of magnitude, from few microns to hundreds of microns. Further tests will be carried out to study even smaller critical defects as well as the role of the microstructure when no specific defect is observed as the cause of fatigue failure.

Acknowledgement

This research was funded by a PhD grant from the French region Pays de la Loire. A special thanks is given to our colleagues from the CEA-LITEN/DTNM/SERE/L3M for L-PBF plates manufacturing, and from the Arts et Métiers (Angers) for specimens and experimental set-up machining.

References

[1] AFNOR, . Nf en 10028-7. URL: https://www.boutique.afnor.org/norme/nf-en-10028-7/produits-plats-en-aciers-pour-appareils-a-pression-partie-7-aciers-inoxydables/article/874486/fa186267.

[2] Andreatta, F., Lanzutti, A., Vaglio, E., Totis, G., Sortino, M., Fedrizzi, L., . Corrosion behaviour of 316L stainless steel manufactured by selective laser melting URL: https://onlinelibrary.wiley.com/doi/abs/10.1002/maco.201910792, doi:10.1002/maco.201910792.

[3] Andreau, O., . Nocivité en fatigue et contrôle de défauts produits par fabrication additive.

[4] Baker, M., Castle, J., . The initiation of pitting corrosion at MnS inclusions 34, 667–682. URL: http://linkinghub.elsevier.com/retrieve/pii/0010938X9390279P, doi:10.1016/0010-938X(93)90279-P.

[5] Baroux, B., . La corrosion des métaux: Passivité et corrosion localisée. Dunod. arXiv:54F2AgAAQBAJ.

[6] Bayat, M., Mohanty, S., Hattel, J.H., . Thermo-fluid-metallurgical modelling of laser-based powder bed fusion process , 7.

[7] Bertsch, K., Meric de Bellefon, G., Kuehl, B., Thoma, D., . Origin of dislocation structures in an additively manufactured austenitic stainless steel 316L 199, 19–33. URL: https://linkinghub.elsevier.com/retrieve/pii/S1359645420305796, doi:10.1016/j.actamat.2020.07.063.

[8] Bhandari, J., Lau, S., Abbassi, R., Garaniya, V., Ojeda, R., Lisson, D., Khan, F., . Accelerated pitting corrosion test of 304 stainless steel using ASTM G48; Experimental investigation and concomitant challenges 47, 10–21. URL: http://linkinghub.elsevier.com/retrieve/pii/S095042301630345X, doi:10.1016/j.jlp.2017.02.025.

[9] Blinn, B., Klein, M., Gläß ner, C., Smaga, M., Aurich, J., Beck, T., . An Investigation of the Microstructure and Fatigue Behavior of Additively Manufactured AISI 316L Stainless Steel with Regard to the Influence of Heat Treatment 8, 220. URL: http://www.mdpi.com/2075-4701/8/4/220, doi:10.3390/met8040220.

[10] Caulfield, B., McHugh, P., Lohfeld, S., . Dependence of mechanical properties of polyamide components on build parameters in the SLS process 182, 477–488. URL: https://linkinghub.elsevier.com/retrieve/pii/S0924013606007886, doi:10.1016/j.jmatprotec.2006.09.007.

[11] Donahue, J.R., Burns, J.T., . Effect of chloride concentration on the corrosion–fatigue crack behavior of an age-hardenable martensitic stainless steel 91, 79–99. URL: http://linkinghub.elsevier.com/retrieve/pii/S0142112316301244, doi:10.1016/j.ijfatigue.2016.05.022.

[12] Duan, Z., Man, C., Dong, C., Cui, Z., Kong, D., wang, L., Wang, X., . Pitting behavior of SLM 316L stainless steel exposed to chloride environments with different aggressiveness: Pitting mechanism induced by gas pores 167, 108520. URL: https://linkinghub.elsevier.com/retrieve/pii/S0010938X19319365, doi:10.1016/j.corsci.2020.108520.

[13] Ebara, R., . Corrosion fatigue crack initiation in 12% chromium stainless steel 468-470, 109–113. URL: http://linkinghub.elsevier.com/retrieve/pii/S0921509307003218, doi:10.1016/j.msea.2006.09.128.

[14] El May, M., Saintier, N., Palin-Luc, T., Devos, O., Brucelle, O., . Modelling of corrosion fatigue crack initiation on martensitic stainless steel in high cycle fatigue regime 133, 397–405. URL: https://linkinghub.elsevier.com/retrieve/pii/S0010938X16303687, doi:10.1016/j.corsci.2018.01.034.

[15] Ernst, P., Newman, R., . Pit growth studies in stainless steel foils. I. Introduction and pit growth kinetics 44, 927–941. URL: http://linkinghub.elsevier.com/retrieve/pii/S0010938X01001330, doi:10.1016/S0010-938X(01)00133-0.

[16] Gibson, I., Rosen, D., Stucker, B., . Additive Manufacturing Technologies. Springer New York. URL: http://link.springer.com/10.1007/978-1-4939-2113-3, doi:10.1007/978-1-4939-2113-3.

[17] Gorsse, S., Hutchinson, C., Gouné, M., Banerjee, R., . Additive manufacturing of metals: A brief review of the characteristic microstructures and properties of steels, Ti-6Al-4V and high-entropy alloys 18, 584–610. URL: https://www.tandfonline.com/doi/full/10.1080/14686996.2017.1361305, doi:10.1080/14686996.2017.1361305.

[18] Guerchais, R., . Influence d'accidents géométriques et du mode de chargement sur le comportement en fatigue à grand nombre de cycles d'un acier inoxydable austénitique 316l.

[19] Hashim, M., Farhad, F., Smyth-Boyle, D., Akid, R., Zhang, X., Withers, P.J., . Behavior of 316L stainless steel containing corrosion pits under cyclic loading 70, 2009–2019. URL: https://onlinelibrary.wiley.com/doi/abs/10.1002/maco.201810744, doi:10.1002/maco.201810744.

[20] Hayashi, M., Amano, K., Ueyama, Y., . Initiation and Growth of Corrosion Pit and Its Effect on Corrosion Fatigue Strength in 12Cr Stainless Steel 66, 957–962. URL: https://www.jstage.jst.go.jp/article/jsms/66/12/66_957/_article/-char/ja/, doi:10.2472/jsms.66.957.

[21] Hlinka, J., Kraus, M., Hajnys, J., Pagac, M., Petrů, J., Brytan, Z., Tański, T., . Complex Corrosion Properties of AISI 316L Steel Prepared by 3D Printing Technology for Possible Implant Applications 13, 1527. URL: https://www.mdpi.com/1996-1944/13/7/1527, doi:10.3390/ma13071527.

[22] Hooper, P.A., . Melt pool temperature and cooling rates in laser powder bed fusion 22, 548–559. URL: https://linkinghub.elsevier.com/retrieve/pii/S221486041830188X, doi:10.1016/j.addma.2018.05.032.

[23] Hu, P., Meng, Q., Hu, W., Shen, F., Zhan, Z., Sun, L., . A continuum damage mechanics approach coupled with an improved pit evolution model for the corrosion fatigue of aluminum alloy 113, 78–90. URL: https://linkinghub.elsevier.com/retrieve/pii/S0010938X16309441, doi:10.1016/j.corsci.2016.10.006.

[24] Kazemipour, M., Nasiri, A., Mohammadi, M., . On Microstructure and Corrosion Properties of Selective Laser Melted 316L Stainless Steel, in: Progress in Canadian Mechanical Engineering, York University Libraries. URL: http://hdl.handle.net/10315/35428, doi:10.25071/10315/35428.

[25] Kong, D., Dong, C., Ni, X., Zhang, L., Luo, H., Li, R., Wang, L., Man, C., Li, X., . The passivity of selective laser melted 316L stainless steel 504, 144495. URL: https://linkinghub.elsevier.com/retrieve/pii/S0169433219333112, doi:10.1016/j.apsusc.2019.144495.

[26] Laleh, M., Hughes, A.E., Xu, W., Cizek, P., Tan, M.Y., . Unanticipated drastic decline in pitting corrosion resistance of additively manufactured 316L stainless steel after high-temperature post-processing , 108412URL: https://linkinghub.elsevier.com/retrieve/pii/S0010938X19320876, doi:10.1016/j.corsci.2019.108412.

[27] Le, V.D., Pessard, E., Morel, F., Edy, F., . Interpretation of the fatigue anisotropy of additively manufactured TA6V alloys via a fracture mechanics approach 214, 410–426. URL: https://linkinghub.elsevier.com/retrieve/pii/S0013794418311664, doi:10.1016/j.engfracmech.2019.03.048.

[28] Leuders, S., Lieneke, T., Lammers, S., Tröster, T., Niendorf, T., . On the fatigue properties of metals manufactured by selective laser melting – The role of ductility 29, 1911–1919. URL: http://www.journals.cambridge.org/abstract_S0884291414001575, doi:10.1557/jmr.2014.157.

[29] Li, R., Liu, J., Shi, Y., Wang, L., Jiang, W., a. Balling behavior of stainless steel and nickel powder during selective laser melting process 59, 1025–1035. URL: http://link.springer.com/10.1007/s00170-011-3566-1, doi:10.1007/s00170-011-3566-1.

[30] Li, S.X., Akid, R., . Corrosion fatigue life prediction of a steel shaft material in seawater 34, 324–334. URL: http://linkinghub.elsevier.com/retrieve/pii/S135063071300280X, doi:10.1016/j.engfailanal.2013.08.004.

[31] Li, Y.F., Farrington, G.C., Laird, C., b. Cyclic response-electrochemical interaction in mono - and polycrystalline AISI 316L stainless steel in H2SO4 solution –II. Potential dependence of the transient dissolution behavior during corrosion fatigue. 41, 709–721.

[32] Lin, L.F., Chao, C.Y., Macdonald, D.D., . A Point Defect Model for Anodic Passive Films: II . Chemical Breakdown and Pit Initiation 128, 1194–1198. URL: https://iopscience.iop.org/article/10.1149/1.2127592, doi:10.1149/1.2127592.

[33] Lodhi, M., Deen, K., Greenlee-Wacker, M., Haider, W., a. Additively manufactured 316L stainless steel with improved corrosion resistance and biological response for biomedical applications 27, 8–19. URL: https://linkinghub.elsevier.com/retrieve/pii/S221486041830873X, doi:10.1016/j.addma.2019.02.005.

[34] Lodhi, M., Deen, K., Haider, W., b. Corrosion behavior of additively manufactured 316L stainless steel in acidic media 2, 111–121. URL: https://linkinghub.elsevier.com/retrieve/pii/S2589152918300401, doi:10.1016/j.mtla.2018.06.015.

[35] Mameng, S.H., Pettersson, R., Leygraf, C., Wegrelius, L., . Atmospheric Corrosion Resistance of Stainless Steel: Results of a Field Exposure Program in the Middle-East 161, 33–43. URL: http://link.springer.com/10.1007/s00501-016-0447-9, doi:10.1007/s00501-016-0447-9.

[36] Mower, T.M., Long, M.J., . Mechanical behavior of additive manufactured, powder-bed laser-fused materials 651, 198–213. URL: http://linkinghub.elsevier.com/retrieve/pii/S092150931530530X, doi:10.1016/j.msea.2015.10.068.

[37] Murakami, Y., . Effects of small defects and inhomogeneities on fatigue strength : Experiments, model and applications to industry , 31–42.

[38] Murakami, Y., Endo, M., . Effects of defects, inclusions and inhomogeneities on fatigue strength 16, 163–182. URL: http://linkinghub.elsevier.com/retrieve/pii/0142112394900019, doi:10.1016/0142-1123(94)90001-9.

[39] Pace, M., Guarnaccio, A., Dolce, P., Mollica, D., Parisi, G., Lettino, A., Medici, L., Summa, V., Ciancio, R., Santagata, A., . 3D additive manufactured 316L components microstructural features and changes induced by working life cycles 418, 437–445. URL: http://linkinghub.elsevier.com/retrieve/pii/S0169433217303458, doi:10.1016/j.apsusc.2017.01.308.

[40] Rajasankar, J., Iyer, N.R., . A probability-based model for growth of corrosion pits in aluminium alloys 73, 553–570. URL: http://linkinghub.elsevier.com/retrieve/pii/S0013794405002614, doi:10.1016/j.engfracmech.2005.10.001.

[41] Riemer, A., Leuders, S., Thöne, M., Richard, H., Tröster, T., Niendorf, T., . On the fatigue crack growth behavior in 316L stainless steel manufactured by selective laser melting 120, 15–25. URL: http://linkinghub.elsevier.com/retrieve/pii/S0013794414000757, doi:10.1016/j.engfracmech.2014.03.008.

[42] Röttger, A., Geenen, K., Windmann, M., Binner, F., Theisen, W., . Comparison of microstructure and mechanical properties of 316 L austenitic steel processed by selective laser melting with hot-isostatic pressed and cast material 678, 365–376. URL: http://linkinghub.elsevier.com/retrieve/pii/S0921509316312205, doi:10.1016/j.msea.2016.10.012.

[43] Saeidi, K., Gao, X., Zhong, Y., Shen, Z., . Hardened austenite steel with columnar sub-grain structure formed by laser melting 625, 221–229. URL: http://linkinghub.elsevier.com/retrieve/pii/S0921509314015056, doi:10.1016/j.msea.2014.12.018.

[44] Sander, G., Thomas, S., Cruz, V., Jurg, M., Birbilis, N., Gao, X., Brameld, M., Hutchinson, C.R., . On The Corrosion and Metastable Pitting Characteristics of 316L Stainless Steel Produced by Selective Laser Melting 164, C250–C257. URL: http://jes.ecsdl.org/lookup/doi/10.1149/2.0551706jes, doi:10.1149/2.0551706jes.

[45] Schaller, R.F., Mishra, A., Rodelas, J.M., Taylor, J.M., Schindelholz, E.J., . The Role of Microstructure and Surface Finish on the Corrosion of Selective Laser Melted 304L 165, C234–C242. URL: http://jes.ecsdl.org/lookup/doi/10.1149/2.0431805jes, doi:10.1149/2.0431805jes.

[46] Schönbauer, B.M., Mayer, H., . Effect of small defects on the fatigue strength of martensitic stainless steels 127, 362–375. URL: https://linkinghub.elsevier.com/retrieve/pii/S0142112319302531, doi:10.1016/j.ijfatigue.2019.06.021.

[47] Shamir, M., Syed, A.K., Janik, V., Biswal, R., Zhang, X., . The role of microstructure and local crystallographic orientation near porosity defects on the high cycle fatigue life of an additive manufactured Ti-6Al-4V 169, 110576. URL: https://linkinghub.elsevier.com/retrieve/pii/S1044580320320477, doi:10.1016/j.matchar.2020.110576.

[48] Trelewicz, J.R., Halada, G.P., Donaldson, O.K., Manogharan, G., . Microstructure and Corrosion Resistance of Laser Additively Manufactured 316L Stainless Steel 68, 850–859. URL: http://link.springer.com/10.1007/s11837-016-1822-4, doi:10.1007/s11837-016-1822-4.

[49] Tsouli, S., Lekatou, A.G., Siozos, E., Kleftakis, S., . Accelerated corrosion performance of AISI 316L stainless steel concrete reinforcement used in restoration works of ancient monuments 188, 03003. URL: https://www.matec-conferences.org/10.1051/matecconf/201818803003, doi:10.1051/matecconf/201818803003.

[50] Wang, Y.M., Voisin, T., McKeown, J.T., Ye, J., Calta, N.P., Li, Z., Zeng, Z., Zhang, Y., Chen, W., Roehling, T.T., Ott, R.T., Santala, M.K., Depond, P.J., Matthews, M.J., Hamza, A.V., Zhu, T., a. Additively manufactured hierarchical stainless steels with high strength and ductility 17, 63–71. URL: http://www.nature.com/articles/nmat5021, doi:10.1038/nmat5021.

[51] Wang, Y.M., Voisin, T., McKeown, J.T., Ye, J., Calta, N.P., Li, Z., Zeng, Z., Zhang, Y., Chen, W., Roehling, T.T., Ott, R.T., Santala, M.K., Depond, P.J., Matthews, M.J., Hamza, A.V., Zhu, T., b. Additively manufactured hierarchical stainless steels with high strength and ductility 17, 63–71. URL: http://www.nature.com/doifinder/10.1038/nmat5021, doi:10.1038/nmat5021.

[52] Wu, Q., Chen, X., Fan, Z., Nie, D., Wei, R., . Corrosion fatigue behavior of FV520B steel in water and salt-spray environments 79, 422–430. URL: http://linkinghub.elsevier.com/retrieve/pii/S1350630716306562, doi:10.1016/j.engfailanal.2017.05.012.

[53] Xie, J., Alpas, A.T., Northwood, D.O., . A mechanism for the crack initiation of corrosion fatigue of Type 316L stainless steel in Hank's solution 48, 271–277. URL: https://linkinghub.elsevier.com/retrieve/pii/S1044580302002450, doi:10.1016/S1044-5803(02)00245-0.

[54] Yadollahi, A., Shamsaei, N., . Additive manufacturing of fatigue resistant materials: Challenges and opportunities 98, 14–31. URL: http://linkinghub.elsevier.com/retrieve/pii/S0142112317300014, doi:10.1016/j.ijfatigue.2017.01.001.

[55] Zerbst, U., Madia, M., Klinger, C., Bettge, D., Murakami, Y., . Defects as a root cause of fatigue failure of metallic components. III: Cavities, dents, corrosion pits, scratches 97, 759–776. URL: https://linkinghub.elsevier.com/retrieve/pii/S135063071830757X, doi:10.1016/j.engfailanal.2019.01.034.

[56] Zhang, M., Sun, C.N., Zhang, X., Goh, P.C., Wei, J., Li, H., Hardacre, D., . Competing influence of porosity and microstructure on the fatigue property of laser powder bed fusion stainless steel 316L , 12.